nature portfolio

https://doi.org/10.1038/s41586-024-08077-6

Supplementary information

Dynamic interface printing

Supplementary Materials for

Dynamic Interface Printing

Callum Vidler[1], Michael Halwes[1], Kirill Kolesnik[1], Philipp Segeritz[1,2,3], Matthew Mail[1], Anders J. Barlow[4], Emmanuelle M. Koehl[5], Anand Ramakrishnan[5,6], Lilith M. Caballero Aguilar[1,7,8], David R. Nisbet[1,7,8,9], Daniel J. Scott[2,3], Daniel E. Heath[1,8], Kenneth B. Crozier[10,11,12], David J. Collins[1,8*]

Affiliations:

[1] Department of Biomedical Engineering, The University of Melbourne, Parkville, Victoria, Australia

[2] The Florey Institute, Parkville, Victoria, Australia

[3] Department of Biochemistry and Pharmacology, The University of Melbourne, Parkville, Victoria, Australia

[4] Materials Characterisation and Fabrication Platform (MCFP), The University of Melbourne, Parkville, Victoria, Australia

[5] Department of Plastic and Reconstructive Surgery, The Royal Melbourne Hospital, Parkville, Victoria, Australia

[6] Department of Surgery, Melbourne Medical School, The University of Melbourne, Parkville, Victoria, Australia

[7] Aikenhead Centre for Medical Discovery, St Vincent's Hospital Melbourne, Fitzroy, Victoria, Australia

[8] The Graeme Clark Institute, The University of Melbourne, Parkville, Victoria, Australia

[9] Faculty of Medicine, Dentistry and Health Science, Melbourne Medical School, The University of Melbourne, Parkville, Victoria, Australia

[10] School of Physics, The University of Melbourne, Parkville, Victoria, Australia

[11] Department of Electrical and Electronic Engineering, The University of Melbourne, Parkville, Victoria, Australia

[12] Australian Research Council (ARC) Centre of Excellence for Transformative Meta-Optical Systems, The University of Melbourne, Parkville, Victoria, Australia

*Corresponding author

E-mail: david.collins@unimelb.edu.au

This PDF File Includes:

Materials and Methods

S1: DIP printing system mechanical design

Version 1

System components were mounted on a pair of orthogonal optical breadboards to facilitate the alignment of the vertical and horizonal components of the system (**Supplementary Fig.2a).** Patterned cross-sections of the object were generated using a high-power projection module (LRS-WQ, Visitech) with a resolution of 2560 x 1600 pixels and pixel size of 15.1 µm. The projection module was mounted to a linear stage (MOX-02-100, Optics Focus), which was affixed to the vertically oriented optical breadboard. Direct control of the dynamic interface was performed via another linear stage (MOX-02-50, Optics Focus) that controlled the displacement of a 50 mL syringe connected to the print head via a silicone hose. An additional pair of linear stages (MOX-02-100, Optics Focus) was used to position the cuvette/well plate below the print head in two dimensions for sequential or multi-step printing. Stage motion control was achieved using a commercially available 3D printer control board (BIGTREETECH, SKR 3) and a custom designed DB9 breakout board to interface with the motion stages.

Orthogonal video of the printing process was captured using a 4K CCD camera (AmScope, HD408) with a 16 mm lens (Raspberry Pi, RPI-16MM-LENS).

Version 2

To incorporate in-situ imaging, a second revision of the system was developed, allowing the probe and associated optical hardware to remain stationary while the printing vessel moved relative to the fixed probe (**Supplementary Fig. 3).** The primary mechanical modifications included the integration of a custom-made coreXY translation system and a NEMA 23 ball-screw linear stage for the z-axis to accommodate the increased vertical payload of the XY gantry. Additionally, a blue reflective dichroic mirror (#35-519, Edmund Optics) and a 50:50 beam splitter (#43-359, Edmund Optics) were added to facilitate in-situ imaging of the interface and structures during fabrication. Illumination for the system can be provided coaxially via an expanded fiber optic light source or through collimated back illumination. In the latter case, this was achieved with a custom-manufactured well-plate or cuvette holder with an integrated red collimated backlight. To maintain physiological temperatures and sterility during printing, the motion components and print head were enclosed within a custom heated chamber. Sterility was ensured by continuous HEPA filtration during printing, surface sanitization with 70% ethanol, and UV-C sterilization prior to use.

Acoustic Modulation

An inline acoustic modulation device was placed between the syringe and the print head which facilitated direct volume manipulation of the air-liquid interface (**Supplementary Fig.2b**). This modulation device consisted of a 3” 15W speaker driver (Techbrands, AS3034) affixed to an enclosed

3D printed manifold containing an inlet and outlet port, such that the speaker cone forms a single side of the enclosed manifold (**Supplementary Fig.1c-d**). The speaker was driven using a 20W audio amplifier (Adafruit, ADA1752) enabling the direct control of the frequency and amplitude of the air-liquid interface via a 3.5 mm auxiliary cable.

S2: Print head design

The print head was tailored to various dimensions, contingent upon the desired dimensions of the resin container. We used axisymmetric cylindrical print heads to simplify the computation of the interface shape, although other (arbitrarily shaped) print head boundary contours were feasible. Print head sizes ranged from D = 25 mm to D = 5 mm. The object's size in the x,y direction was limited by the projector's total field of view at the focal plane and the object height was limited by the length of the print head, which in our case was equal to the projection focal length. For our setup, the total submergible print head length was approximately 70 mm. Much taller structures would be feasible by submerging the projection and illumination optics, or by demagnifying the projection optics in order to increase the working distance. The print head consisted of 6 parts, which when combined created an enclosed air-volume with a glass window at its top to enable light transmission down its centre **(Supplementary Fig.1a-b).** Additionally, a pneumatic channel located on the side of the print head enables direct pressurization and acoustic excitation of the air-liquid boundary. All components were 3D printed using a commercial resin 3D printer (Formlabs, Form3+).

S3: Software control

A custom MATLAB GUI was used to control the DIP printing system which enabled the voxelization of STL geometries, pre-processing of image arrays using the convex slicing algorithm, motion control via G-code over a serial data connection, video capture, video transmission to the projection module over HDMI, projection module control, and acoustic modulation. Printing of structures was performed by first generating a waveform for each degree of freedom of the interface, whereby the global position of the interface was dependent on the summation of all waveforms. This approach allowed us to create highly complex motion control as shown in **Fig.1c.**

S4: Air-liquid interface modelling

In DIP, the shape of the interface can be approximately described by the Young-Laplace equation which relates the interface curvature to the differential pressure sustained across the boundary. In general, this can be written as the following:

$$\Delta p = -\gamma \nabla \cdot \hat{n}, \tag{1}$$

where Δp denotes the Laplace pressure, γ is the surface tension and $\hat{n}$ is the vector normal to the surface. Following the approach from Butt *et al.*[1], the shape of the non-dimensionalized interface can be found by substituting the general expressions for the principal curvatures[2] of an axisymmetric surface as shown below:

$$p_i - \rho g z = \gamma \left(\frac{r''}{(1+r'^2)^{\frac{3}{2}}} - \frac{1}{r\left(1+r'^2\right)^{\frac{1}{2}}} \right), z \in (0, h). \tag{2}$$

The coordinate origin is taken as the contact point of the meniscus edge with the print head, with the positive z-axis being directed downward along the print head's central axis and the r-axis parallel to the print-head's diameter. The superscript prime denotes the derivative with respect to z, and h denotes the maximum height of the meniscus given by:

$$\frac{h}{R_o} = 2(Bo)^{-\frac{1}{2}} \sin\left(\frac{\theta_Y}{2}\right), \tag{3}$$

where R_o is the radius of the theoretical spherical meniscus with volume $V_o = \frac{4\pi}{3} R_o^3$, Bo denotes the bond number and θ_Y is the contact angle. Therefore, the shape of the meniscus can be determined via numerical integration of the above non-linear second order ODE. The integration starts at $z = 0$ to the point $z = h$, with the initial radius and radial slope equal to the print head radius and contact angle, respectively. Additionally, the solution is constrained such that the volume of the meniscus must match the total volume of air injected into the print head. To solve this, we chose to frame the Young-Laplace equation as an initial value problem, using an implementation of the shooting method in MATLAB[2]. The solution for this problem was defined with initial values that satisfy the following boundary constraints:

$$\mathbf{M} = \left\{ \begin{matrix} r(0) - R \\ r'(0) - \cot(\theta_Y) \\ \pi \int_0^h r^2 dz - V_o \end{matrix} \right\} = 0. \tag{4}$$

This therefore converts the above boundary value problem into a root finding solution which aims to ensure that the boundary conditions $\mathbf{M} = 0$. A comparison between the curvature of the interface determined numerically and experimentally is shown in Supplementary **Fig.3a**, wherein the Young-Laplace model accurately predicts the interface curvature for an increasing internal pressure state p_i.

It is worth noting that the shape of the interface depends on the quantity $p_i - \rho g z$, where p_i denotes the pressure within the print head. As the print head is withdrawn from the bath, the value of $\rho g z$ decreases linearly and therefore the value of p_i must also change linearly to maintain the same interface shape.

S5: Convex interface formation

As the DIP approach relies on the pressurization of a print container to produce an air-liquid meniscus, the profile of this boundary and consequently the cured region is non-planar. Traditional slicing schemes[3] assume that the projected geometry is parallel to the construction plane and as such would result in reconstructed artefacts in the case of DIP. To correct for this in the case of an axisymmetric print head, the three-dimensional surface can be reconstructed by revolving the Young-Laplace predicted surface about the z-axis (**Supplementary Fig.4b**). Let the discrete interface profile, $Z(r)$, be the solution to the boundary value problem, with the parametric expression of the reconstructed 3D surface given by:

$$x(\theta, r) = r\cos\theta, \tag{5}$$

$$y(\theta, r) = r\sin\theta, \tag{6}$$

$$z(\theta, r) = Z(r). \tag{7}$$

S6: Voxel intersection

Unlike standard DLP printing, the projected images required for DIP arise from the intersection of a convex surface with the voxelized representation of the target geometry, resulting in a non-planar slicing scheme. The voxels which lie on this surface can be determined via a distance minimization of the surface to the voxel in the array. Let a point on the surface of the interface be defined by $S_p = (x_p, y_p, z_p)$ such that it satisfies the above parametric relationship, and the voxel representation of the desired model is given by $[V_i, V_j, V_k]$, where i, j, k represent the dimensions of the voxel matrix whose i, j dimensions define the number of corresponding pixels in-plane and the maximum size of k is determined by the discretization of the object as a function of the sliced layer height. Additionally, $[V_i, V_j, V_k]$ represents a binary 3D matrix where the presence of geometry is defined by a '1' and the absence of geometry is defined by a '0'. Whether a voxel is located on the surface of the interface (S_p) is determined by the minimization of the Euclidian distance between that point and the closest voxel. If n voxels are present within the same Euclidian distance, then the resultant value is averaged over n samples in the following way:

$$\breve{V} = \frac{1}{n}\sum_{n=1}^{n} \arg\min_{i,j,k}, V \tag{8}$$

where $\breve{V}$ represents the voxel coordinate and value which satisfies the above relationship. This approach is repeated for each location on the interface in three-dimensional space, where the desired image sent to the projection module for each layer is given by:

$$I_{ij}^{k} = \|\breve{V}\|, \tag{9}$$

where $\|\breve{V}\|$ denotes the voxel value and the superscript k denotes the projection in the sequence. This relationship represents the equivalent projection of the three-dimensional voxel array onto the interface surface in two dimensions. It's worth noting that as the voxel array has been reduced to two dimensions via the projection, therefore we have lost some information about its original position. To preserve this, we also store the absolute original z-location of the pixels for each projection, which becomes useful later for reconstruction:

$$IZ_{ij}^{k} = \breve{V}_k\,, \tag{10}$$

where IZ is the matrix containing the absolute z-locations and $\breve{V}_k$ denotes the global z-coordinate of the pixel stored in I_{ij}^{k}. As the print head moves up in the positive z-direction, the voxels intersected by the interface changes. To determine this intersection, the interface profile is translated in the z-direction corresponding to the discretization of the voxel array (layer height = L_h) in the z-direction:

$$z(\theta, r) = Z(r) + L_h. \tag{11}$$

S7: Determining the intermediate interface shape

To ensure the printed object remains adhered to the print container, the meniscus must be flattened against the bottom surface such that the maximum extent of the printed part, R_{max}, is contained within the flat region of the meniscus. To predict the extent to which the print head must be lowered to create said flat region, a Bézier curve method for approximating the meniscus shape is used as previously described[4,5]. Briefly, a MATLAB script minimizes the error of the Young-Laplace equation for a meniscus in a cylindrical capillary at a print head position corresponding to an undeformed meniscus, which is defined via the control points of a Bézier curve. The print head position is then moved downwards, and the free control points are moved radially outwards in a stepwise fashion until the height of the meniscus at $\mathrm{R_{max}}$ is approximately 0, while preserving the meniscus volume **(Supplementary Fig.4a**). To solve for the initial meniscus shape, a dimensionless form of the Young-Laplace equation is used:

$$\frac{\frac{d^2y}{dx^2}}{\left(1+\left(\frac{dy}{dx}\right)^2\right)^{\frac{3}{2}}}+\frac{\frac{dy}{dx}}{x\left(1+\left(\frac{dy}{dx}\right)^2\right)^{\frac{1}{2}}}-y=0, \tag{12}$$

where $x=\frac{r}{l}$, $y=\frac{h}{l}$, and $l=\sqrt{\frac{\sigma}{\rho g}}$ is the capillary length. The above equation is solved using the boundary conditions $\frac{dy}{dx}=0$ at $\mathrm{x}=0$ and $\frac{dy}{dx}=cot\,\theta_Y$ at $x=x_3$, where x_3 is the dimensionless form of the print head radius and θ_Y is the contact angle.

To solve the above equation, a cubic Bézier curve is defined along with its first and second derivatives:

$$B(t)=(1-t)^3P_0+3(1-t)^2tP_1+3(1-t)t^2P_2+t^3P_3, \tag{13}$$

$$B'(t)=3(1-t)^2(P_1-P_0)+6(1-t)t(P_2-P_1)+3t^2(P_3-P_2), \tag{14}$$

$$B''(t)=6(1-t)(P_2-2P_1+P_0)+6t(P_3-2P_2+P_1), \tag{15}$$

where t is a parametric variable and $P_0, P_1 \dots P_n$ represent the control points of the Bézier curve. After defining the x- and y-coordinates of the control points, MATLAB is used to calculate the *x,y* coordinates of the meniscus curve as well as the first and second derivatives. Then, $\frac{dy}{dx}$ and $\frac{d^2y}{dx^2}$ are calculated using the following equations:

$$\frac{dy}{dx}=\frac{\frac{dy}{dt}}{\frac{dx}{dt}}, \tag{16}$$

$$\frac{d^2y}{dx^2}=\frac{\left(\frac{dx}{dt}\right)\left(\frac{d^2y}{dt^2}\right)-\left(\frac{dy}{dt}\right)\left(\frac{d^2x}{dt^2}\right)}{\left(\frac{dx}{dt}\right)^3}. \tag{17}$$

Afterwards, a loss term is defined corresponding to the sum of the dimensionless Young-Laplace equation divided by the sum of the y-coordinates of the meniscus curve. The undeformed meniscus shape is then calculated using the MATLAB function fminsearch. Once this “steady-state” solution is found, the flattened meniscus shape is calculated by moving the control point P_3 (corresponding to the edge of the print head) down. Control points P_1 and P_2 are then moved radially outward and the meniscus shape is solved again, preserving the arc length of the meniscus so that meniscus volume is maintained. This is repeated until the meniscus height at R_{max} is close enough to 0 as evaluated by a user-defined threshold.

Aside from remapping the 3D cartesian geometry in order to slice the volume with a curved print interface, the meniscus shape presents an additional challenge for the beginning layers of the print. If we define the first layer of the print where the air/liquid interface was lowered into the container using the "steady state" meniscus shape, any geometry of the desired object radially beyond the contact point C (**Supplementary Fig. 5a**) could not be cured correctly. The height of the air/liquid interface at all points between $r = 0$ and $r = R_{max}$ (the maximum extent of the object's base) would be too tall, and this would lead to (1) the print not adhering to the container bottom and (2) the print not correctly matching the desired geometry. Therefore, the air/liquid interface must be lowered past this initial contact point, deforming the interface to form a (pseudo) flat region.

The number of interpolation steps used is dependent on the discretization of the volume (V_k) and the layer height L_h. One challenge with applying such an approach for predicting the slicing profile within this interpolated region is that the solution is comprised of a series of overlapping surfaces wherein a voxel can be incident with more than one surface. To combat this, two approaches can be used to ensure that a single voxel and subsequently the projections that make up that voxel never result in a value that exceeds the target original value. One way to do this could be to reduce the greyscale value I_{ij}^k, such that its cumulative dosage never exceeds $\|\breve{V}\|$. However, if the number of interpolation steps exceeds 255, the solution lacks sufficient degrees of freedom. This is further complicated by the fact that the curing propagation rate R_p scales non-linearly with intensity[6]:

$$R_p = \frac{k_p}{k_t^{1/2}}[M](\phi I_a)^{1/2}, \tag{18}$$

where k_p and k_t represent the propagation and termination parameters of the material, $[M]$ is the initial monomer concentration, ϕ is the quantum yield and I_a is the absorbed intensity, which in our case is proportional to the greyscale value described in I_{ij}^k. A more convenient approach is to exclude those voxels that have already been written by the interpolated surface from the voxel array. This approach solves both the degree of freedom constraint imposed by an 8-bit image and the non-linear intensity threshold which governs curing onset. Therefore, the available voxels for each loop can be written as the following, where k represents the interpolation step over the domain $(0, z')$, with:

$$[V_i, V_j, V_k]^{k+1} = [V_i, V_j, V_k]^k - \|\overbrace{V_{ijk}}\| .$$

S8: Geometry reconstruction from projections

To validate that the convex slicing algorithm results in the same input geometry, the generated projections are traced back through an empty target volume (**Supplementary Fig.5d**). For each image in the projection sequence of size k, the voxel value is determined by the quantity I_{ij}^k, whose global position in the matrix is determined by IZ_{ij}^k. Let V' be an empty target volume with dimensions equal to the input geometry $[V_i', V_j', V_k'] = 0$. Therefore, any element in V' is given by the coordinate transform of the projection sequence such that:

$$V_{ijk}' = [I_{ij}^k, IZ_{ij}^k], \ \|V_{ijk}'\| = \ \|I_{ij}^k\|. \tag{19}$$

S9: Computing the reconstruction error (δ)

The similarity between the reconstructed volume and the input volume was computed using the Jaccard Index. For each 2D orthogonal component plane of the volume, the Jaccard Index[7] was summed over the volume and averaged over each component axis, whereby:

$$J(V', V) = \frac{1}{3}\left(\frac{1}{i}\sum_{i=1}^{i} \frac{V_{jk}'^{i} \cap V_{jk}^{i}}{V_{jk}'^{i} \cup V_{jk}^{i}} + \frac{1}{j}\sum_{j=1}^{j} \frac{V_{ik}'^{j} \cap V_{ik}^{j}}{V_{ik}'^{j} \cup V_{ik}^{j}} + \frac{1}{k}\sum_{k=1}^{k} \frac{V_{ij}'^{k} \cap V_{ij}^{k}}{V_{ij}'^{k} \cup V_{ij}^{k}}\right) = \delta, \quad \delta \in [0,1]. \tag{20}$$

The reconstruction error is thus quantified by a single value $\delta \in [0,1]$, which determines the similarity between the target domain and the computed domain, where a value of $\delta = 1$ denotes a perfect match. A low value of δ normally denotes an interface step size mismatch between the voxel representation V and the layer slice height L_h. Therefore, the slicing step size was reduced until the Jaccard Index exceeded a threshold value $\bar{\delta}$ which in our case was set $\bar{\delta} > 0.9$. A process flow diagram of this slicing scheme can be found in **Supplementary Fig.5e**.

S10: Theoretical model of optical resolution

In the case of DIP, print resolution is determined by exposure energy density, magnification, spatial distribution of the projection optics, and the photo-polymer response, which depends on photo-initiator concentration, monomer concentration and photo-absorber concentration. To quantify the theoretical resolution of the imaging system, we employed a similar approach outlined by Behroodi et al.[8] which predicts the final energy distribution at the projection plane as the superposition of the point-spread functions of all pixels reflected from the DMD surface via spatial convolution:

$$f(x,y) * PSF(x,y) = \int_{\tau_1=-\infty}^{\infty} \int_{\tau_2=-\infty}^{\infty} f(\tau_1, \tau_2) \ \cdot PSF(x-\tau_1, y-\tau_2) d\tau_1 d\tau_2, \tag{21}$$

where $f(x,y)$ denotes the spatial function of the micromirror cross section at the projection plane. For a single pixel on the DMD, the spatial function is determined by:

$$f(x,y) = \begin{cases} \frac{g_s}{255} - m\frac{d_x}{2} < x < m\frac{d_x}{2}, -m\frac{d_y}{2} < y < \frac{d_y}{2} \\ 0x < \ -m\frac{d_x}{2}, m\frac{d_x}{2} < x, y < \ -m\frac{d_y}{2}, m\frac{d_y}{2} < y \end{cases}, \tag{22}$$

where d_x and d_y denote the dimensions of the micromirror, m is the magnification of the projection optics and g_s denotes the greyscale value $[0, 255]$. The spatial convolution equation determines the equivalent Gaussian distribution function (ω_0) at the focal plane of the projection optics. The diameter of the point on the focal plane can subsequently be modelled by the Gaussian distribution, where the UV intensity of a point source at a given plane is defined by:

$$I(x,y,z) = \frac{2P}{\pi[\omega(z)]^2} e^{\frac{-2(x^2+y^2)}{[\omega(z)]^2}}, \tag{23}$$

where $I(x, y, z)$ is the optical intensity of the projected light with units $(\mathrm{J/cm^2s})$, P is the total power of the UV light determined in units of $(\mathrm{J/s})$ and $\omega(z)$ denotes the Gaussian radius at a location z, whose half-width is $1/e^2$ of the Gaussian maximum intensity I_{max}. In the case of DIP for an axisymmetric print head, the curvature of the meniscus imposes a radially symmetric change in the Gaussian radius dependent on the meniscus height $Z(r)$. As $Z(r)$ was initially determined from an origin located at the print head, an equivalent profile $X_m(z)$ will be implemented such that $X_m(0) = 0$ and $X_m(z) = \max Z(r)$, this ensures that the maximum meniscus deformation is coincident with the image plane when $z = 0$, **Supplementary Fig.6a**. The Gaussian beam width at a location on the meniscus is therefore given by:

$$\omega(z) = \omega_o\sqrt{1 + \left(\frac{X_m(z)}{Z_R}\right)^2}, Z_R = \frac{\pi n \omega_0^2}{\lambda}, \tag{24}$$

where ω_0 denotes the beam waist, n is the refractive index and λ is the wavelength. Therefore, the exposure energy per unit area for a finite time t and meniscus surface is:

$$E(x, y, z, t) = I(x, y, z)t.$$

S11: Energy density across the meniscus

Light entering the resin through the surface of the meniscus is either absorbed or scattered by the material. These two effects determine the fraction of energy deposited into the material and therefore the polymerization thickness and penetration depth. From Beer-Lambert, the energy per unit area within the resin surface is governed by an exponential reduction in intensity based on material parameters[9]

$$E(x, y, z, z', t) = E(x, y, z, t)\, e^{\frac{-z\prime}{D_p}}, \;\; D_p = \frac{1}{\varepsilon_d[D] + \varepsilon_i[S]}, \tag{25}$$

where D_p is the penetration depth at which the intensity falls to $1/e^2$ of the surface intensity, ε_d and ε_i are the molar absorption coefficients of the photo-initiator and photoabsorber, respectively, D and S are the concentrations of the photo-initiator and photo-absorberand z' defines the coordinate system into the material which is not necessarily aligned with the optical axes. In the case of DIP, the curvature of the meniscus decomposes the incoming light at the location (x, y, z) into scattered and transmitted components. At any location z on the meniscus surface, the incident angle of the incoming ray of light can be defined by α_0 relative to the print head axis. In our case $\alpha_0 \approx 0$, however, it could be feasible that $\alpha_0 \neq 0$ for some print head and optical configurations. Similarly, the angle of the meniscus α_m and its normal $\widehat{\alpha_m}$ at location (x, y, z) relative to the print head axis can be determined by:

$$\alpha_m = \tan^{-1}\left(\frac{dX_m(z)}{dz}\right), \;\; \widehat{\alpha_m} = \pi - \cot^{-1}\left(\frac{dX_m(z)}{dz}\right), \tag{26}$$

where $X_m(z)$ denotes the radial position of the meniscus as a function of the meniscus height z. The definition of this ray in three-dimensions coincident with a point on the surface of the meniscus (x, y, z), can be approximately described by the Gaussian-beam theory[10]. Under the assumption of an axisymmetric print head, the normal vector at this point in-two dimensions $\hat{\boldsymbol{n}}$ and associated light ray $\hat{\boldsymbol{u}}$, is given by:

$$\hat{\boldsymbol{u}} = \langle \cos \alpha_0 , \sin \alpha_0 \rangle, \tag{27}$$

$$\hat{\boldsymbol{n}} = \langle \cos \widehat{\alpha_m} , \sin \widehat{\alpha_m} \rangle. \tag{28}$$

From Snell's Law, the angle of the outgoing ray relative to the surface normal is given by the relative change in the refractive index of the material and the incident angle θ_1. As the angle between the incoming ray $\hat{\boldsymbol{u}}$ and surface normal $\hat{\boldsymbol{n}}$ is given by the dot product $\cos \theta_1 = \hat{\boldsymbol{u}} \cdot \hat{\boldsymbol{n}}$, the outgoing angle θ_2 relative to the surface normal can be simplified to the following:

$$\theta_2 = \sin^{-1}\left(\frac{n_1}{n_2}\sqrt{1-(\hat{\boldsymbol{u}} \cdot \hat{\boldsymbol{n}})^2}\right). \tag{29}$$

The direction of this ray represents the new coordinate system $\hat{\boldsymbol{\gamma}}$ for the Beer-Lambert solution where the rotation of the ray with respect to the local coordinate system vector $\hat{\boldsymbol{z}} = \langle \mathbf{1}, \mathbf{0} \rangle$ is given by:

$$\alpha_{\hat{\gamma}} = \pi - \cot^{-1}\left(\frac{dX_m(z)}{dz}\right) + \sin^{-1}\left(\frac{n_1}{n_2}\sqrt{1-(\hat{\boldsymbol{u}} \cdot \hat{\boldsymbol{n}})^2}\right), \tag{30}$$

$$\alpha_{\hat{\gamma}} = \pi - \cos^{-1} \hat{\boldsymbol{z}} \cdot \hat{\boldsymbol{n}} + \sin^{-1}\left(\frac{n_1}{n_2}\sqrt{1-(\hat{\boldsymbol{u}} \cdot \hat{\boldsymbol{n}})^2}\right), \tag{31}$$

$$\hat{\boldsymbol{\gamma}} = \langle \cos \alpha_{\hat{\gamma}} , \sin \alpha_{\hat{\gamma}} \rangle, \tag{32}$$

where the new coordinate axes for the Beer-Lambert solution are given by:

$$\langle \boldsymbol{\gamma}_x, \boldsymbol{\gamma}_y, \boldsymbol{\gamma}_z \rangle = \langle \widehat{\boldsymbol{\gamma}_\perp}, \widehat{\boldsymbol{\gamma}_\perp} \times \hat{\boldsymbol{\gamma}}, \hat{\boldsymbol{\gamma}} \rangle. \tag{33}$$

Furthermore, the proportion of light transmitted into the material is dependent on the incident angle θ_1 and the energy per unit area $E(x, y, z, t)$. Using the Fresnel equations[11], the transmission coefficients for parallel and perpendicular polarizations are proportional to the cosine of the incoming and outgoing rays, such that:

$$T_\perp = \frac{2n_1 \cos \theta_1}{n_1 \cos \theta_1 + n_2 \cos \theta_2}, \tag{34}$$

$$T_{||} = \frac{2n_1 \cos \theta_1}{n_2 \cos \theta_1 + n_1 \cos \theta_2}. \tag{35}$$

Under the assumption that the incoming light is not polarized, the transmission coefficient T is given by the average of the S and P polarization states. As the Fresnel coefficients represent amplitudes, the transmitted intensity η at the ray-meniscus intersection is proportional to the square of the amplitude:

$$T = \frac{T_\perp + T_{||}}{2}, \tag{36}$$

$$\eta = T^2. \tag{37}$$

The energy per unit area E is dependent on the position of the incoming ray $\hat{\boldsymbol{u}}$, its coordinate system is such that $\hat{\boldsymbol{z}} \cdot \hat{\boldsymbol{u}} \approx 1$ and $\hat{\boldsymbol{x}} \cdot \hat{\boldsymbol{u}} \approx 0$. In general, under the assumption that the beam's half-width is not sufficiently large and where the gradient at the surface $\left[\frac{\partial z}{dx}, \frac{\partial z}{dy}\right]$ ensures that $\Delta z_{-\omega_0}^{\omega_0} \approx 0$, then the vector $\hat{\boldsymbol{E}}$ can be shown to be:

$$\hat{\boldsymbol{E}} \approx \hat{\boldsymbol{u}} \cdot E(x, y, z). \tag{38}$$

Similarly, if $\hat{\boldsymbol{n}}$ defines the normal vector at the meniscus, then the transmitted component $\mathcal{H}(\boldsymbol{\gamma}_x, \boldsymbol{\gamma}_y, \boldsymbol{\gamma}_z)$ with coordinates relative to the transmissive beam, is given by

$$\mathcal{H}\left(\boldsymbol{\gamma}_x, \boldsymbol{\gamma}_y, \boldsymbol{\gamma}_\mathbf{z}\right) = \eta(n_1, n_2, \widehat{\boldsymbol{u}}, \widehat{\boldsymbol{n}}) \cdot \widehat{\boldsymbol{E}}\, e^{\frac{-\gamma_Z}{\varepsilon_d[D]+\varepsilon_i[S]}}\,.$$

S12: Modelling the effective resolution, meniscus working region and interfacial focal map.

The effective printing resolution can be formed by convolving the point spread function over a single pixel, wherein the theoretical point spread function in three-dimensions can be simulated by defocusing in the Fourier domain by a modulated Gaussian function, where:

$$\widehat{\boldsymbol{h}}(\omega, z) = e^{-\sigma(z)^2\omega^2 \cdot \frac{\sin\zeta(\omega,z)}{\zeta(\omega,z)}}, \tag{39}$$

$$\zeta(\omega, z) = \frac{\zeta \cdot \omega(1-\omega)}{K(z_i - z)}. \tag{40}$$

This approach results in the 3D representation of the point spread function as shown in **Supplementary Fig.6b**. Therefore, the effective pixel size was approximated over a *z*-range of 5 mm towards the projection lens. By assuming that the allowable pixel size can only deviate by $\sqrt{2}P_{xy}$, where P_{xy}denotes the in-plane pixel size, the effective meniscus region can be plotted for varying print head sizes and material surface tensions, **Supplementary Fig.6c**. It's worth noting that the entirety of the meniscus can be used as demonstrated by the convex slicing algorithm, however, the spatial resolution is dependent on the curvature and its relative location away from the optical axis. To investigate the theoretical defocusing of a projected image in the plane, the standard USAF test pattern was convolved at $z = 0\ \mathrm{mm}, z = 3\ \mathrm{mm}$, and $z = 5\ \mathrm{mm}$, **Supplementary Fig.6d**.

To investigate the effective reduction in resolution across the meniscus, a checkerboard pattern was computed at numerous regions between 0 – 5 mm. By comparing the relative height of the interface at the location (x, y, z) to the corresponding pixel in the defocused checkerboard array, the effective defocused pixel representation was generated across the entirety of the interface as shown in **Supplementary Fig.6e**.

S13: Derivation and modelling of capillary waves on the air-liquid boundary:

During printing, a thin fluid volume of uncured material is created between the meniscus and the previously cured region, the height of which depends on the oxygen inhibition zone of the material[12,13] and the *z*-translation of the meniscus. The Navier-Stokes continuity and momentum equations for incompressible Newtonian fluids can be written as:

$$\rho\left(\frac{\partial \boldsymbol{u}}{\partial t} + (\boldsymbol{u} \cdot \nabla)\boldsymbol{u}\right) = -\nabla \boldsymbol{T} + \rho \boldsymbol{g} \tag{41}$$

$$\rho \nabla \cdot \boldsymbol{u} = 0, \tag{42}$$

where ρ is the fluid density, $\boldsymbol{u}$ denotes the velocity, $\boldsymbol{T} = -p\boldsymbol{I} + \mu(\nabla\boldsymbol{u} + (\nabla\boldsymbol{u})^T)$ is the stress tensor, p is the pressure, and μ is the dynamic viscosity, $\boldsymbol{g}$ is the standard gravity. From lubrication theory[14–16], a thin fluid volume or film can be described under the assumption that the fluid depth is much shallower than the fluid's extent. Under this assumption, the full Navier-Stokes equations can be simplified. As the velocity at small length-scales is small compared to the viscous forces, the inertial terms on the left hand-side are negligible as they are proportional to u^2/L. This approximation reduces the momentum equation to $0 = -\nabla p + \rho \boldsymbol{g} + \mu \nabla^2 \boldsymbol{u}$. Furthermore, as the thickness of the film is assumed to be small, the velocity perpendicular to the plane is negligible. For the case of an axisymmetric print head, the coordinate system is such that $\boldsymbol{x}$ denotes the vector in the radial direction, $\boldsymbol{z}$ denotes the vector parallel to the optical axis, and $\mathbf{y}$ denotes the vector perpendicular to $\boldsymbol{xz}$, resulting in the following reduced momentum equations:

$$-\frac{dp}{dx} + \mu \frac{\partial^2 u}{\partial z^2} = 0, \tag{43}$$

$$-\frac{dp}{dy} + \mu \frac{\partial^2 v}{\partial z^2} = 0, \tag{44}$$

$$-\frac{dp}{dz} + \rho g = 0. \tag{45}$$

For a thin-film under incompressible flow, the increase in volumetric flow rate in the positive x-direction is given by:

$$\Delta Q = \left[\int_0^{h(x)} u dz\right]_x^{x+\Delta x}. \tag{46}$$

where $h(x)$ is the meniscus height. This must be balanced by the decrease in volumetric flow in the z-direction, $-\frac{\partial h}{\partial t} dx$. By assuming a non-slip condition at the previously printed interface and finite shear across the boundary, the horizontal velocity profile is given by:

$$u = \frac{1}{\mu} \frac{\partial p}{\partial x} \left(\frac{z^2}{2} - hz\right) + \frac{\tau}{\mu} z. \tag{47}$$

Equating the volumetric flow rate yields,

$$\frac{\partial Q}{\partial x} = \frac{\partial}{\partial x} \int_0^{h(x)} u dz = -\frac{\partial h}{\partial t}, \tag{48}$$

$$\frac{\partial}{\partial x} \int_0^{h(x)} \left(\frac{1}{\mu} \frac{\partial p}{\partial x} \left(\frac{z^2}{2} - hz\right) + \frac{\tau}{\mu} z\right) dz = -\frac{\partial h}{\partial t}, \tag{49}$$

$$\frac{\partial}{\partial x} \left(\frac{1}{\mu} \frac{\partial p}{\partial x} \left(\frac{-h^3}{3}\right) + \frac{\tau}{\mu} \frac{h^2}{2}\right) = -\frac{\partial h}{\partial t}, \tag{50}$$

$$\tau h \frac{\partial h}{\partial x} + \frac{h^2}{2} \frac{\partial \tau}{\partial x} - \frac{1}{3} \frac{\partial}{\partial x} \left(h^3 \frac{\partial p}{\partial x}\right) = -\mu \frac{\partial h}{\partial t}. \tag{51}$$

In our case, the volume of air within the print head is acoustically driven, causing a variation of pressure and shear force along the surface of the meniscus which is proportional to the local air pressure and velocity. The pressure in a sound wave is given by $P = P_0 + A \sin(\omega t - Kx)$, where the velocity is in-phase with the pressure $v = B \sin(\omega t - Kx)$, where A and B depend on factors such as the compressibility of the air and the amplitude of the wave. The pressure within the fluid can now be described by the following:

$$p - p_{atm} = \rho g h - \gamma \frac{d^2 h}{dx^2} + A \sin(\omega t - Kx) + f(z). \tag{52}$$

Inserting this into the above equation for the shear force and applying the assumption of small perturbations in the interface height $h = h_0 + \varepsilon$, the equation can be linearized as shown.

$$B\sin(\omega t - Kx)\,h\frac{\partial h}{\partial x} - \frac{h^2}{2}BK\cos(\omega t - Kx) - \frac{1}{3}\frac{\partial}{\partial x}\left(h^3\left(\rho g\frac{\partial h}{\partial x} - \gamma\frac{d^3h}{dx^3} - KA\cos(\omega t - Kx)\right)\right) = -\mu\frac{\partial h}{\partial t}, \tag{53}$$

$$B\sin(\omega t - Kx)\,h_0\frac{\partial \varepsilon}{\partial x} - \frac{h_0^3}{3}\left(\rho g\frac{\partial^2\varepsilon}{\partial x^2} - \gamma\frac{d^4\varepsilon}{dx^4}\right) + \mu\frac{\partial\varepsilon}{\partial t} = \frac{h_0^2}{2}BK\cos(\omega t - Kx) - \frac{h_0^3}{3}K^2A\sin(\omega t - Kx). \tag{54}$$

If B is negligible, then the meniscus would only be affected by the pressure from the acoustic driver, and not the shear from the driver. Under this assumption, the above equation can be solved analytically and simplified to the following:

$$\frac{h_0^3}{3}\left(\rho g\frac{\partial^2\varepsilon}{\partial x^2} - \gamma\frac{d^4\varepsilon}{dx^4}\right) - \mu\frac{\partial\varepsilon}{\partial t} = \frac{h_0^3}{3}K^2A\sin(\omega t - Kx). \tag{55}$$

The homogenous solution to the above equation is of the form $\varepsilon = Ce^{ikx+st}$, where the constant s describes the relaxation of the disturbance given by $s = \frac{-h_0^3}{3\mu}(\rho g k^2 + \gamma k^4)$. The particular solution should also be of the form $F\sin(\omega t - Kx) + G\cos(\omega t - Kx)$. Therefore, substituting this in gives the particular solution of,

$$\varepsilon_p = A_p(3\mu\omega\cos(\omega t - Kx) - h_0^3K^2(\rho g + \gamma)\sin(\omega t - Kx)), \tag{56}$$

$$A_p = \frac{Ah_0^3K^2}{K^4h_0^6(\rho g+\gamma)^2 + 9\omega^2\mu^2}. \tag{57}$$

The time dependent solution to a small perturbation in the interface height ε, can be determined by adding together the homogeneous and particular solutions resulting in an equation that describes the full solution of meniscus perturbation under acoustic sound waves,

$$\varepsilon = \mathrm{e}^{-\frac{h_0^3}{3\mu}(\rho g k^2+\gamma k^4)t}(C_1\cos\ kx + C_2\sin\ kx) + A_p(3\mu\omega\cos\,(\omega t - Kx) - h_0^3K^2(\rho g + \gamma)\sin\,(\omega t - Kx)). \tag{58}$$

This equation describes the time dependent solution to the interface height as a function of the acoustically driven perturbations of the interface, whereby the produced waves are added to waves caused by previous perturbations that decay exponentially in time. It's worth noting that this solution can only accurately be applied for low frequency acoustic perturbations (like those used in this work), as the inertial terms in the momentum equation have been assumed to be negligible. Under high frequency acoustic driving, the fluid element would need to change position much faster than what is captured by this model, in this instance the components $\frac{\partial \boldsymbol{u}}{\partial t}$ and $\boldsymbol{u}\cdot\nabla\boldsymbol{u}$ would be non-zero. Inserting this back into the equation for the velocity in the x-direction, yields:

$$u = \frac{\rho g}{\mu}\frac{\partial\varepsilon}{\partial x}\left(\frac{z^2}{2} - (h_0 + \varepsilon)z\right), \tag{59}$$

$$\frac{\partial\varepsilon}{\partial x} = \mathrm{e}^{-\frac{h_0^3}{3\mu}(\rho g k^2+\gamma k^4)t}(-kC_1\sin\ kx + kC_2\cos\ kx) + A_p(h_0^3K^3(\rho g + \gamma)\cos\,(Kx - \omega t) - 3K\mu\omega\sin(Kx - \omega t)), \tag{60}$$

$$u = \frac{\rho g}{\mu}\left(\mathrm{e}^{-\frac{h_0^3}{3\mu}(\rho g k^2+\gamma k^4)t}(-kC_1\sin kx + kC_2\cos kx) + A_p(h_0^3K^3(\rho g + \gamma)\cos(Kx - \omega t) - 3K\mu\omega\sin(Kx - \omega t))\right) \times \left(\frac{z^2}{2} - \left(h_o + \left(\mathrm{e}^{-\frac{h_0^3}{3\mu}(\rho g k^2+\gamma k^4)t}(C_1\cos\ kx + C_2\sin\ kx) + A_p(3\mu\omega\cos\,(\omega t - Kx) - h_0^3K^2(\rho g + \gamma)\sin\,(\omega t - Kx))\right)\right)\right). \tag{61}$$

In the above equation, the constants C_1 and C_2 describe the amplitudes of previous evolutions of the wave, k is the wave number, K is the dimensionless wavenumber which is normalized against the capillary length $\frac{K}{L_{cap}}$, ω is the driving frequency, γ is the surface tension, ρ is the density and A_p is the driving amplitude. Note that this approximate model of the interface dynamics does not take into account the streaming effects generated by the meniscus curvature nor the squeeze flow due to the translation of the air-liquid interface in the z-direction, **Supplementary Fig.19a-c**. The result from the image based de-wetting analysis shown **Supplementary Fig.11** indicates that the influx rate of material under acoustic stimulation is approximately an order of magnitude higher than under lubrication-driven flow. Therefore, we can approximate the material influx rate based on acoustics alone as a conservative estimate. Furthermore, to account for the curvature of the interface, the constant fluid depth h_0 is replaced by $h(x)$ which describes the height of the meniscus as a function of the print head's diameter, **Supplementary Fig.19d-e.**

S14: Scaling laws for acoustically driven flows

To understand how fluid transport is affected by different material parameters, we can assume the interface height in an idealized case is given by $h(x,t) = h_0 + \phi(t)\cos(qx)$, where q denotes the wavenumber and $\phi(t)$ describes the amplitude of the wave. Under this approximation, the pressure within the fluid is given by the atmospheric pressure, gravitational effects and capillary effects. For lubrication theory to hold, the relative height change of the interface is small compared to its depth, therefore the curvature of the interface can be approximated by $\kappa = d^2h/dx^2$. The pressure difference between the crest and the trough scales with $\gamma\phi/\lambda^2$ in the capillary case and with $\rho g\phi$ in the gravity-driven case. We can therefore describe the ratio of gravitational to capillary effects as $\lambda^2\rho g/\gamma$ or $\left(\lambda/l_{cap}\right)^2$, whereby $\left(\lambda/l_{cap}\right)^2 > 1$ denotes a system where gravity dominates and $\left(\lambda/l_{cap}\right)^2 < 1$ denotes a system where capillary effects dominate[17]. Using this relationship, in conjunction with the generalized equation for velocity in the x-direction, we can derive a scaling relationship for the velocity U dependent on material parameters. By using a length scale of λ in the *x*-direction and h_0 in the *z*-direction, it can be shown that:

$$U \propto \frac{h_0^2\rho g\phi}{\lambda\mu}, \text{for } \left(\frac{\lambda}{l_{cap}}\right)^2 \gg 1, \tag{62}$$

$$U \propto \frac{h_0^2\gamma\phi}{\lambda^3\mu}, \text{for } \left(\frac{\lambda}{l_{cap}}\right)^2 \ll 1, \tag{63}$$

where the wavelength λ is found by solving the dispersion relation for capillary waves, which relates the wave frequency (ω) to the wavenumber (k) and is given by:

$$\omega^2 = \frac{\gamma}{\rho}k^3 + gk. \tag{64}$$

An example of these scaling laws can be shown for different material processing parameters in **Supplementary Fig.19f-g**.

S15: Effect of interface curvature on streaming flows

When acoustically driving the meniscus profile under low amplitude oscillations for increasing internal pressure states, we observed a dramatic increase in fluid flow below the interface when compared to a pseudo-level interface, **Supplementary Fig.10**. We postulate that this enhanced fluid transport is driven by two key factors related to the meniscus curvature and an increase in available mass volume. Firstly, following the analysis by Prinet *et al*. and Zhong *et. al*[18,19], the streaming velocity below the meniscus can be written as a function of the parallel streaming velocity,

$$\boldsymbol{u_s}|_{z=\zeta_0} = -\frac{3}{4\omega}\hat{u}_{\parallel}^2\partial_\tau\hat{u}_{\parallel}\hat{\boldsymbol{t}}, \tag{65}$$

where $\hat{u}_{\parallel}$ denotes the primary flow parallel to the meniscus, $\hat{\boldsymbol{t}}$ denotes the tangential vector to the meniscus and ζ_0 describes the surface elevation of the static meniscus, whose solution is given by the Young-Laplace equation. The value for the tangential velocity at the meniscus surface $\hat{u}_{\parallel}$ is obtained through linear interpolation of the meniscus wave along the meniscus at $z = \zeta_0(x)$:

$$\hat{u}_{\parallel} = -\cos\,\omega t \sum_n^\infty A_n k_n \frac{1+k_n\zeta_0}{[1+(\partial_x\zeta_0)^2]^{1/2}}(\sin\,k_n x - \partial_x\zeta_0\cos\,k_n x), \tag{66}$$

where k_n describes the eigen-wavenumber $k_n = n\pi/\lambda$, the coefficient $A_n = \frac{2\omega a_0}{\omega^2-\omega_n^2}\frac{(-1)^n+s}{(m^2+k_n^2)\lambda}$, a_0 is the forcing acceleration, s is the interface symmetry and m is the mode number in the y-direction. Substituting in the equation for $\hat{u}_{\parallel}$, the meniscus streaming velocity can be written as:

$$\boldsymbol{u_s}|_{z=\zeta_0} = \left\{-\frac{3}{4\omega}\sum_{n,m} A_n A_m(k_n + \zeta_0 k_n^2)(k_m + \zeta_0 k_m^2)\left[k_m - \frac{\rho g_0}{\sigma}(\zeta_0 - z\,*)\right]\sin(k_n x)\cos(k_m x) + O(\partial_x\zeta_0)\right\}\hat{\boldsymbol{\imath}} + O(\partial_x\zeta_0)\hat{\boldsymbol{\jmath}}, \tag{67}$$

where $\hat{\boldsymbol{\imath}}\text{ and }\hat{\boldsymbol{\jmath}}$ denote the horizontal and vertical unit vectors. Therefore, $\boldsymbol{u_s}$ is intrinsically dependent on the interface profile ζ_0, which produces a periodic streaming profile anchored about the two nodal positions in the case where the meniscus profile is symmetric. The resulting streaming magnitude is therefore dependent on the Fourier spectrum of the static meniscus profile as highlighted by Zhong *et. al,* wherein the flow profile is shaped by the entire wave spectrum rather than a single monochromatic wave. Therefore, for a given frequency and amplitude, the curvature defines a velocity excitation mode, the magnitude of which depends on the shape of the interface. In addition to the meniscus curvature, we also hypothesize that for an increasing meniscus profile beyond the extent of the print head the available material influx scales with:

$$Q \propto \int_0^\kappa \zeta_0(x)\,dx, \tag{68}$$

where κ denotes the maximum extent of the interface from the print head edge. The value of Q will increase up until the point that $\partial_x\zeta_0|_{z=\kappa} = \cot\theta_Y$. Beyond this point the interface keeps increasing in volume laterally, however, the value of κ does not substantially increase. We hypothesize that this lateral volume expansion is due to manufacturing inaccuracies in the print head, which result in lateral translation and rotation of the contact line producing a slightly wider and obtuse meniscus than the diameter of the print head. This overpressurization results in three key changes that impact the efficacy of the interface to induce streaming. Firstly, as the volume of the meniscus increases, we obtain an effective amplitude reduction due to the increase in internal volume. Furthermore, the contact line rotation produces a positive bulged region, which limits material influx due to flow separation and destructive flow interactions. Finally, the ‘stiffness’ of the bubble in the x-direction decreases in comparison to the z-direction, resulting in both vertical and horizontal driving modes, reducing the overall efficiency.

S16: Interface wetting model

The rate at which you can print in DIP is primarily dependent on two key processing parameters, the responsiveness of the material to light and the rate at which new material can enter the printing interface. For the former, the polymerization kinetics are driven by the intensity of light, monomer concentration, oxygen inhibition region, photo absorber concentration and photo-initiator concentration[20]. For the latter, the rate of material influx is driven primarily by the velocity of the interface in the z-direction and the frequency and amplitude of acoustic driving. However, an important criterion to meet is to ensure that, independent of the part geometry, the interface is completely saturated with new material. To predict this infill time for a given geometry we employ a computational approach based on the distance transform of the voxel array[21], where the presence of geometry is defined as a ‘1’ and the absence of geometry is defined by ‘0’. We can, therefore, treat the ‘0’ regions in the voxel array as resin sources, which define the fluidic path length. For each voxel in the array the distance between a white pixel $w_{i,j,k}$ and the closest source $s_{i,j,k}$ is given by,

$$D_{i,j,k} = \arg\min_{i,j,k} \sqrt{(w_i - s_i)^2 + \left(w_j - s_j\right)^2 + (w_k - s_k)^2}. \tag{69}$$

Therefore, the time to until the voxel $w_{i,j,k}$ is completely filled with new material is approximately

$$t = \beta \frac{D_{i,j,k}}{\vec{u}}. \tag{70}$$

where t represents the infill time, $D_{i,j,k}$ is the magnitude of the distance between the voxel $w_{i,j,k}$ and the closest source $s_{i,j,k}$ and β represents a correction factor which depends on the geometry, material properties and volume of the available source material. Additionally, two constraints are applied to the solution $D_{i,j,k}$ which depend on the object geometry and interface shape. The first is that for a given voxel $w_{i,j,k}$, the search region for the closest source point cannot exceed k, as k defines the printing surface. Source regions greater than k contain no material as they exist above the air-liquid meniscus. Secondly, a source point is only valid if the vector between the source and the voxel $\vec{V}_{s\to w}$, does not intersect the geometry, **Supplementary Fig.13a**. This is to ensure that a minimum solution is not found which is blocked by neighbouring geometry. This approach is quite similar to voxel ray tracing, which is often used in computer graphics for modelling light transport[22,23]. For example, let $\vec{V}_{s\to w}$ be the vector formed between $w_{i,j,k}$ and $s_{i,j,k}$, whose distance is given by $D_{i,j,k}$. The origin of the vector $O(O_i, O_j, O_k)$ be located at the source $s_{i,j,k}$, with a direction vector $D\left(D_i, D_j, D_k\right)$, therefore any point along the vector its position is given by.

$$P = O + tD. \tag{71}$$

Let the bounding box of the voxel array, be given by $V_{min} = \left(V_{min,i}, V_{min,j}, V_{min,k}\right)$ and $V_{max} = \left(V_{max,xi}, V_{max,j}, V_{max,k}\right)$. To determine if the ray intersects the voxel, we compute the intersection points with the planes defining the voxel's surfaces. For each voxel face we compute the entrance and exit points of the ray:

$$t_{enter,i} = \frac{V_{min,i} - O_i}{D_i}\ , t_{exit,j} = \frac{V_{min,i} - O_i}{D_i}\ , \tag{72}$$

$$t_{enter,j} = \frac{V_{min,j} - O_j}{D_j}\ , t_{exit,j} = \frac{V_{min,j} - O_j}{D_j}\ , \tag{73}$$

$$t_{enter,k} = \frac{V_{min,k} - O_k}{D_k}\ , t_{exit,j} = \frac{V_{min,k} - O_k}{D_k}\ . \tag{74}$$

The ray intersects the voxel if and only if the intervals (t_{enter}, t_{exit}) for each axis overlap. The intersection occurs if the maximum value among all t_{enter} values is less than or equal to the minimum value among all t_{exit} values. If an intersection is found, its position can be calculated by using the value of t over the interval in which the intersection occurred.

S17: Print speed prediction using interface wetting model

Using the interface wetting model, the fluidic path length and wetting time can be determined for representative slice planes, as shown in **Supplementary Fig. 13b-c**. By repeating this approach for all object planes (**Supplementary Fig. 13e**) and taking the maximum value for each plane, the fluidic path length D_z, interface wetting t_z time and vertical print velocity V_z (independent of curing kinetics) can be generated over the entire object (**Supplementary Fig. 13f**). Therefore, two independent solutions for an object's print time can be created. Firstly, a conservative approach can be applied wherein the print speed is dependent on the minimum V_z value over the entire object. Alternatively, the print speed can be dynamically increased or decreased in a geometrically dependent way based on the local V_z of that layer. A comparison between the cumulative print time of these two approaches can be shown in **Supplementary Fig. 13g**.

S18: Finite element analysis of the printing resin influx

To analyse the effects of the curved interface and acoustic actuation on printing speed, we model printing material inflow using finite element analysis (FEA) software COMSOL Multiphysics 6.1. Resin ingress across printing structure was investigated for two competing printing schemes: the DIP (**Supplementary Fig.20a-b**) and the classic top-down stereolithography printing approach (**Supplementary Fig.20c-d**). We employ axial symmetry of the problem by utilizing 2D axisymmetric modeling domains to drastically reduce computational effort. The print head and printed structure are treated as impermeable solids and excluded from the modeling.

The Laminar Flow module is used to model the pressure and velocity field in the printing material (PEGDA) and air subdomains. Assuming incompressible Newtonian fluids, this module utilize the

Navier-Stokes equations. A non-slip boundary condition is used on all the outer walls of the domains except the free surface and the meniscus. For initial conditions, velocity components are zero and a zero reference pressure is induced at the top boundary. The air properties were set at a density of 1.204 kg/m^3 and a viscosity of 18.1 μPas. The PEGDA density was 1012 kg/m^3. Viscosity and surface tension data for PEGDA can be found in **Table 1**.

PEGDA-air interface and PEGDA free surface are simulated with the Moving Mesh module. The velocity and the normal stress boundary condition on the PEGDA-air interface are set as following:

$$\boldsymbol{u_1} = \boldsymbol{u_2}. \tag{75}$$

$$(\boldsymbol{T_1} - \boldsymbol{T_2})\boldsymbol{\hat{n}} = \gamma(\nabla_s \boldsymbol{\hat{n}})\boldsymbol{\hat{n}}. \tag{76}$$

where indices 1 and 2 denote the PEGDA and the air phases respectively, $\boldsymbol{\hat{n}}$ is the unit normal, outward from the PEGDA domain, and $\nabla_s = (\boldsymbol{I} - \boldsymbol{\hat{n}}\boldsymbol{\hat{n}^T})\nabla$ is the surface gradient operator. The Moving Mesh interface enables spatial displacement of the corresponding domain boundaries in response to the fluid motion. It utilizes the arbitrary Lagrangian-Eulerian (ALE) formulation where the mesh grid mapping to the material domain enables solving a deforming Lagrangian-type systems [COMSOL Multiphysics Reference Manual, Version 6.1]. The Navier-Stokes equations are solved within a moving frame, fully coupled with the mesh equations. The mesh velocity normal component thus matches the normal fluid velocity on the boundary. In the case of a free surface, the expressions can be simplified accordingly.

A preliminary study is conducted to establish the shape of the PEGDA-air meniscus. To do it we use a domain which has no printed structure, and the meniscus equilibrium shape is evaluated by running a time-dependent study with stationary boundary conditions (zero boundary displacement). In the subsequent analysis, the shape of the formed meniscus defines the profile of the printed structure.

To model the transient fluid ingress during printing, a dynamic study is conducted. As an initial state, the interface is considered compressed against the printed structure, forming a uniform 50 μm thick layer of fluid. This was chosen to improve initial computational stability of the solution, especially under acoustic excitation. Selected boundaries are translated downward (along the z-axis) as shown in **Supplementary Fig. 20a,c,** to replicate the displacement of the print head during the printing process. While the print head is translated upwards in the experiment, the modeling set-up is inverted and the resin container with the printed structure is displaced down instead. The displacement is performed with a delay of 0.1 s necessary for the computational model stabilization (**Supplementary Fig. 20e**). In the acoustically driven case, the upper part of the air domain is harmonically actuated at $f = 100$ Hz in addition to the displacement. The wall velocity has an amplitude of 10 mm/s and a delay of 0.1 s (**Supplementary Fig. 20f**), necessary for model stabilization.

The computational domain mesh, shown in **Supplementary Fig. 21a-b**, utilizes a hybrid grid with triangular mesh elements in the bulk of the domain, complemented with a structural grid at the fluid ingress area and near nonslip boundaries. The mesh is finely resolved at the structure tip down to $d_{mesh} = 8$ μm and expands to $72d_{mesh} = 0.57$ mm in the bulk of the domain.

The air-fluid interface aligns with the printed structure surface at the start of the simulation. The deformation of the domain propels the meniscus detachment from the structure. The displacement of the meniscus centroid C is plotted in **Supplementary Fig. 21c** for DIP with the printed structure of $S_D = 10$ mm. In the timeframe 0.1-0.96s, it translates downwards, following the boundary displacement. However, the fluid ingress along the structure causes the rebound of the meniscus and subsequent recovery. The rebound dynamics was used to evaluate the computational mesh where the half-sized mesh demonstrates practically identical dynamics of the meniscus.

Supplementary Fig.23-24 plots the fluid velocity and velocity vectors across the approximate influx timeframe for four cases: Top-Down SLA, DIP without acoustics, DIP with acoustics driven at 40 Hz and DIP with acoustics driven at 100 Hz. These figures demonstrate an intensive flow in the interface layer adjacent to the structure. The acoustic actuation was found to induce pressure variation in the air domain with an amplitude of about 20 Pa. This pressure oscillation induces capillary-gravity waves at the liquid-air interface. **Supplementary Fig.24** demonstrates resulting fluid streaming along the acoustically actuated fluid-gas interface, ultimately accelerating the resin influx. The PEGDA ingress in turn induces recirculating flow in adjacent air domain. Acoustics actuation subsequently reduces the time required for complete wetting of the structure.

Supplementary Fig.26a-b plots the oscillation modes of the acoustically actuated meniscus. This visualization demonstrates the complex interactions between meniscus shape, print head size and printed structure size which governs the oscillation intensity and eventually the fluid ingress. While this study is limited to an axisymmetric case, more complex spatial modes might be observed in 3D system. These findings underline the importance of multimodal surface actuation to ensure efficient resin influx.

S19: Particle image velocimetry (PIV)

A key component of the Dynamic Interface Printing technology is the velocity profile below and across the curved air-liquid interface. The complex nature of this system is such that the flow profile is intrinsically determined by the driving frequency, meniscus curvature, print head geometry, material properties, proximity to a solid boundary and the underlying structure of this boundary (whether printed or otherwise). The mathematical approaches discussed in previous sections aim to elucidate some of the primary driving mechanisms for acoustically driven flow. Like any model, however, they cannot capture the full extent of this behaviour.

To supplement our mathematical explanation, we used 2D particle image velocimetry (PIV) to observe the flow behaviour from both the top (**Supplementary Fig.8**) and side (**Supplementary Fig.9**) profiles of the air-liquid interface. The flow profile created by the air-liquid boundary extends in three-dimensions, therefore we aimed to capture key components of this flow profile by sectioning the interface about the xy and xz planes.

PIV imaging, laser and material setup

The PIV illumination setup consisted of a 200 mW 523nm green laser which was subsequently passed through a 45° Powell Lens (Thorlabs, LGL145) to create a uniform sheet of light. To adjust the thickness of the far-field beam, a second cylindrical lens (Thorlabs, LJ1629L2) was placed between the Powell lens and the cuvette resulting in approximately a 300 μm thick sheet at the focal plane. The focal plane of the light sheet was adjusted such that it intersected the mid-plane of the print head (yz) and the beam divergence was assumed to be negligible over the extent of the cuvette. For the side PIV experiments, the length of the light sheet was aligned such that it bisected the print head in the xz plane. For the top-down PIV experiments, the light sheet was rotated 90° and aligned just below the maximum extent of the meniscus.

High speed images of the interface dynamics and interfacial fluid flow were captured using a Chronos 1.4 camera (Kron Technologies, Chronos 1.4 Camera) which enabled a maximum framerate of 40,413 fps. In our case, the camera framerate was varied from 200 – 2000 fps, depending on the experimental conditions. For both the side and top-down PIV experiments a microscope lens was used (Kron Technologies, Microscope lens), and the magnification of the lens was set to ensure the entire ROI was in-view.

20-50μm PMMA particles (LaVision, PMMA particles 20-50 μm) were used to seed the flow at a density of 0.1% (w/v). All PIV experiments were performed using a 25 mm diameter print head with a 20% PEGDA formulation without the photo initiator or photo-absorber to ensure adequate light-transmission through the volume. Particle detection was therefore determined by florescent excitation and scattering of the light sheet.

PIV Analysis

The recorded high-speed video was analyzed using PIVLab within MATLAB. For each experimental condition, a binary mask was generated to isolate the fluid region. In the top-down experiments, the mask corresponded to the diameter of the print head, and for the side-profile experiments the mask covered the print head body and maximum meniscus extent. The maximum meniscus extent was determined by edge tracking of the interface over the time series. The mask was therefore determined to be the maximum location of the interface at any point within the time series + 10%. This was to ensure that the interface movement did not contribute to the velocity profile. This approach potentially results in a lower measured maximum fluid velocity than in reality, though, as the flow close to the interface is truncated by the mask. Additionally, movement of the interface during acoustic actuation produces periodic lensing which precludes accurate PIV tracking, especially at high amplitudes. Therefore, the velocity profile was calculated approximately 90 ms after acoustic stimulation was turned off, which corresponds to the approximate interface settling time in the fluid bulk (**Supplementary Fig. 7**). Therefore, the calculated velocity in this case is lower than when acoustic stimulation is on. For each image in the video sequence, the following PIVLab settings were used:

1. ROI was determined by the binary mask.
2. Each image was pre-processed with the CLAHE filter (10px), high-pass filter (45px) and denoise filter (5px). The contrast was set to auto and the mean background was subtracted from each image.
3. The PIV analysis was performed with the default settings with an integration area of 64px and a step of 32px. A second pass integration area of 32px and a step of 16px was also performed.
4. Both velocity vector validation and image-based validation were used to remove vectors outside 2x the standard deviation of the vector-field.

The final velocity values V_x, V_y and $||V||$ were exported from PIV lab and recreated within MATLAB. The resulting top-down and side-view PIV data is shown in **Supplementary Fig. 8** and **Supplementary Fig. 9.**

S20: Interface release dynamics

One experimental challenge with investigating the fluid release rate close to an interface using PIV is that the fluidic displacement caused by the air-liquid boundary removes tracer particles from the region of interest. This is further exemplified by the fact that the curved oscillating boundary scatters incoming light generated by the light-sheet, resulting in image processing artefacts. As an alternative method to track the material influx rate, we doped each corresponding material with a small volume fraction of black dye and placed the cuvette on top of a bright backlight to produce a uniform light source beneath the cuvette. When the interface is in contact with the bottom of the cuvette, the dyed material is evacuated below the interface resulting in a clear circular contact region, **Supplementary Fig. 11a**. As the print head begins to move up in the z-direction, material flows in to fill available space resulting in a high contrast circle that reduces in diameter as a function of time, **Supplementary Fig. 11b**. By fitting an ellipsoid around the high-contrast region, the proportion of dry area (white areas) to wet areas (black areas) can be plotted as a function of time for acoustic and non-acoustic stimulation, **Supplementary Fig. 11c-d**. The average fluid velocity $\mathrm{V}_{\mathrm{fill}}$, for a period of time is given by:

$$\mathrm{V}_{\mathrm{fill}} = \sqrt{\frac{a_i - a_f}{\Delta t_{i\to f}} + \frac{b_i - b_f}{\Delta t_{i\to f}}}, \tag{77}$$

where, a, b denote the principal axes of the ellipsoid and i, f denote the initial and final values over the time point $\Delta t_{i\to f}$.

S21: Particle settling in dynamic interface printing

A significant obstacle in employing low-viscosity materials for cell-laden biofabrication arises from the dependency of cellular sedimentation rates on the relative densities of the materials involved and the viscosity of the bath material. The settling velocity of a spherical particle is proportional to $v \propto \Delta\rho\mu^{-1}$. In practice this causes a density-driven migration of particles towards the base of the structure prior to printing. To investigate this effect, we suspended 30 µm PMMA particles which have a density of $\sim 1.2\ \mathrm{g/cm^2}$, into a solution of 20% PEGDA with a density approximately that of water $\sim 1.2\ \mathrm{g/cm^2}$, and a viscosity of $\sim 3\ \mathrm{mPa \cdot s}$. The PEGDA-particle mixture was then left for approximately 30 minutes to ensure that the majority of particles had settled to the base of the container prior to printing. To evaluate particle distribution in the final construct, a 10 mm diameter, 20 mm tall rod was printed with and without acoustic stimulation. After printing, the rod was sectioned in the xz plane and imaged using an inverted microscope (**Supplementary Fig. 15a-c**). The location and distribution of particles in the sectioned plane was determined by thresholding, segmenting the image into a binary array and summating the intensity in the *x* and *y* directions of the image (**Supplementary Fig. 15d-e**).

In both cases, DIP mitigated the effect of particle settling even without acoustic stimulation. Particles were distributed throughout the rods, though in the case without acoustic stimulation, the density of particles decreased sharply above the bottom layers. We postulate that the size of the print head relative to the diameter of the cuvette (approximately ½) causes secondary flows due to the print head retraction from the volume, which aid in resuspending particles into the bulk material. Under acoustic excitation, this resuspension is further improved by circulating flows generated across the extent of the print head. In addition to the improved resuspension, the greater material influx rate under acoustic stimulation not only improves the distribution of particles in the z-direction, but also increases the total number of encapsulated particles. This is highly useful for biofabrication, wherein a greater number of cells could be encapsulated within the construct for the same cell density.

S22: Optical power measurements

Optical power measurements were taken at the focal plane of the projection module using a commercial optical power meter (PM100A, Thorlabs) with a 200 -1100 nm Si photodiode (S120VC, Thorlabs). To determine the optical power density, a 900 µm aperture was placed in front of the photodiode.

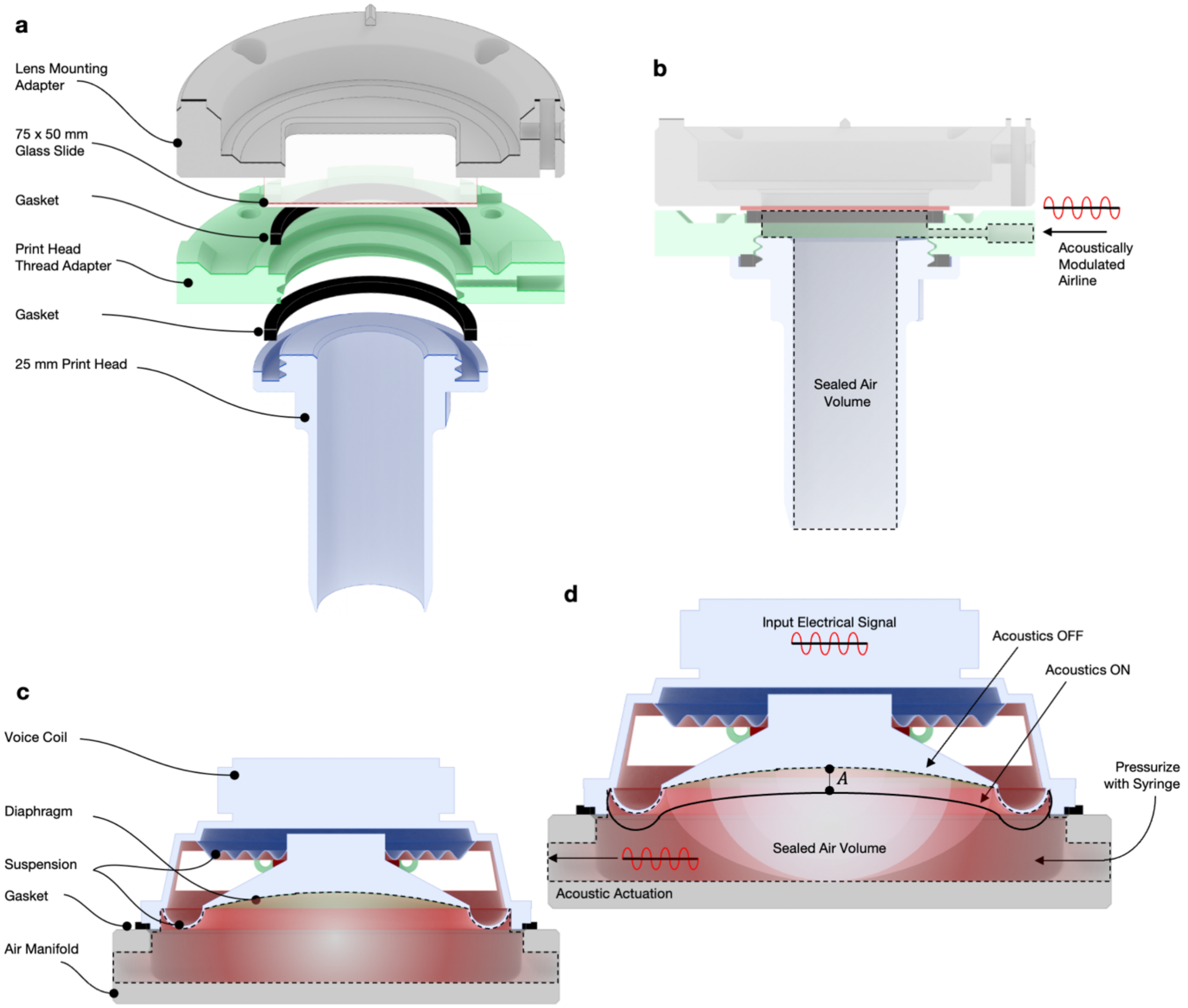

Supplementary Fig.1 | Illustrated CAD model of the print head assembly and acoustic air-line modulation. **a**, expanded half section view of the print head assembly. **b**, collapsed half section view of the print head assembly, highlighting that a sealed air-volume is formed with a transparent glass window at the top. **c**, half section view of the air-line modulation system, wherein a speaker diaphragm forms one side of an enclosed box. **d**, electrical signal applied to the voice coil causes excitation of the diaphragm which modulates the volume around a set point pressure within the air-manifold and in turn the print head.

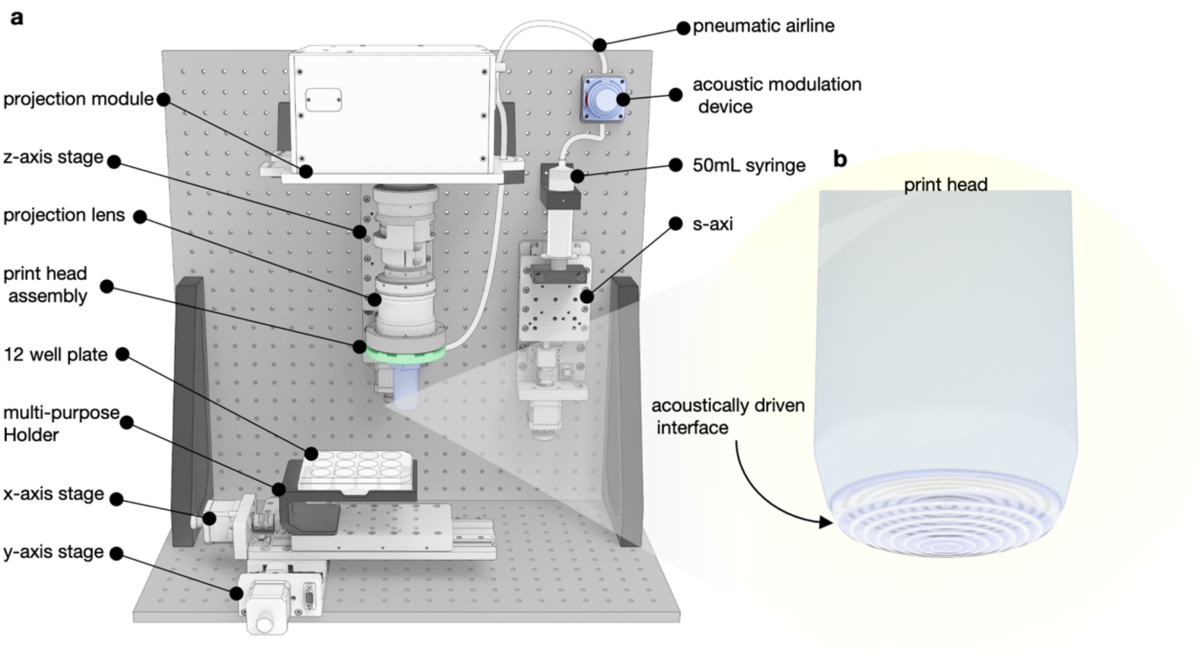

Supplementary Fig.2| Illustrated CAD model of the mechanical components of the DIP printing system version 1 (V1). a, labelled components of the prototype DIP system. **b,** inset view of an air-liquid boundary formed at the tip of the print head under acoustic excitation.

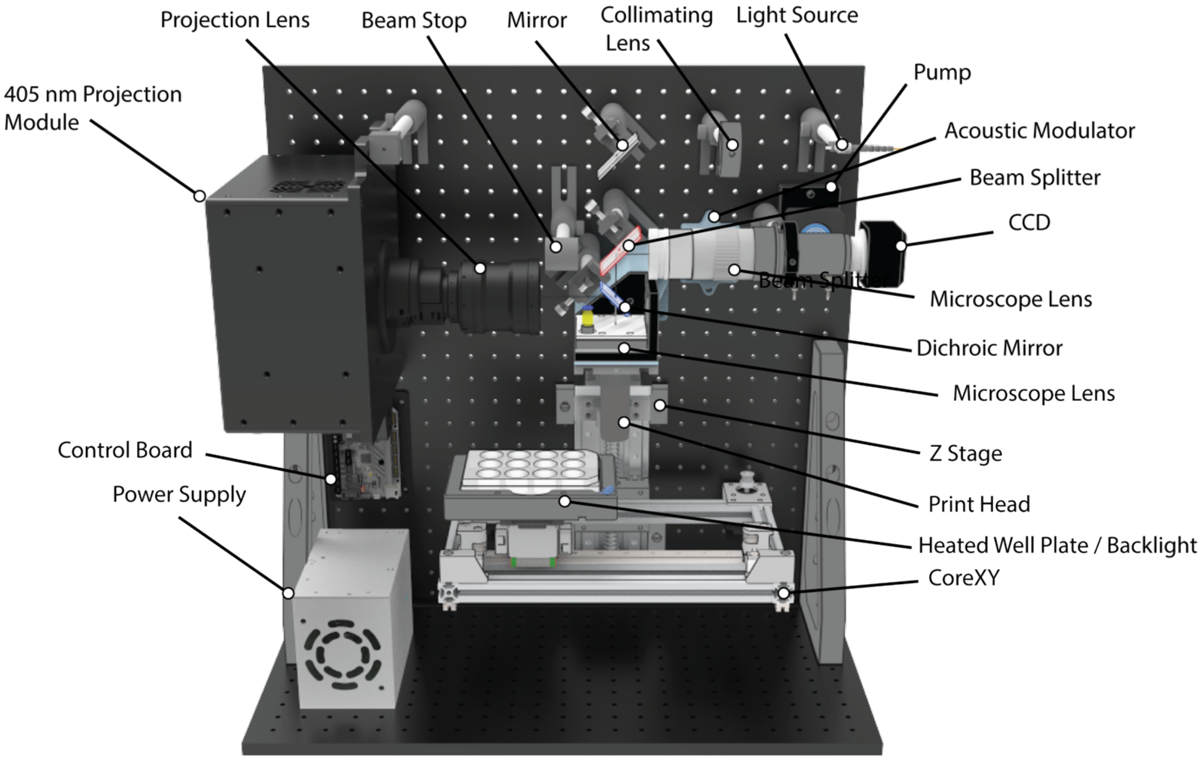

Supplementary Fig.3 | Illustrated CAD model of the mechanical components of the DIP printing system version 2 (V2). Version 2 of the DIP system builds upon the same principles as V1, however adds additional capabilities for in-situ imaging and a larger XY printing area.

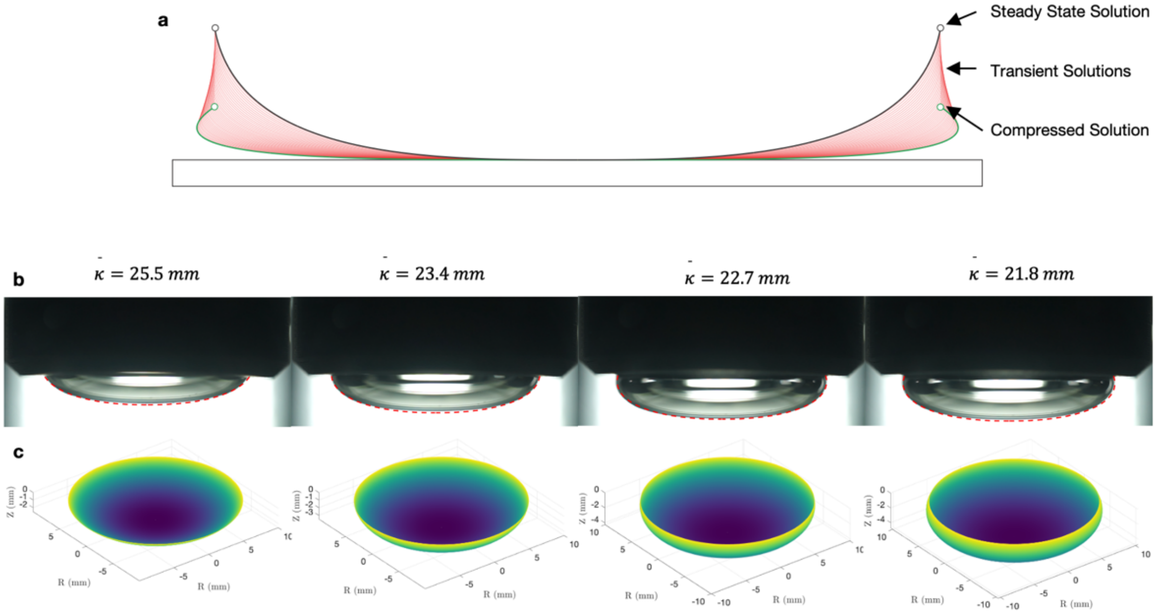

Supplementary Fig.4 |Interface shape reconstruction based on Bezier Young-Laplace model. a, solutions of the approximated Young-Laplace equation using Bezier curves as the interface transitions from a steady-state solution to the compressed solution, for a given pseudo-flat diameter. **b**, shape of the air-liquid meniscus formed at the tip of a 20 mm print head. Red dashed line indicates the solution from the Bezier Young-Laplace model overlayed with the real-world curvature. $\bar{\kappa}$ indicates the average radius of curvature for each interface, where for increasing pressure difference ΔP the interface curvature $\bar{\kappa}$ decreases. **c**, three-dimensional reconstruction of the interface profile assuming symmetry about the z-axis.

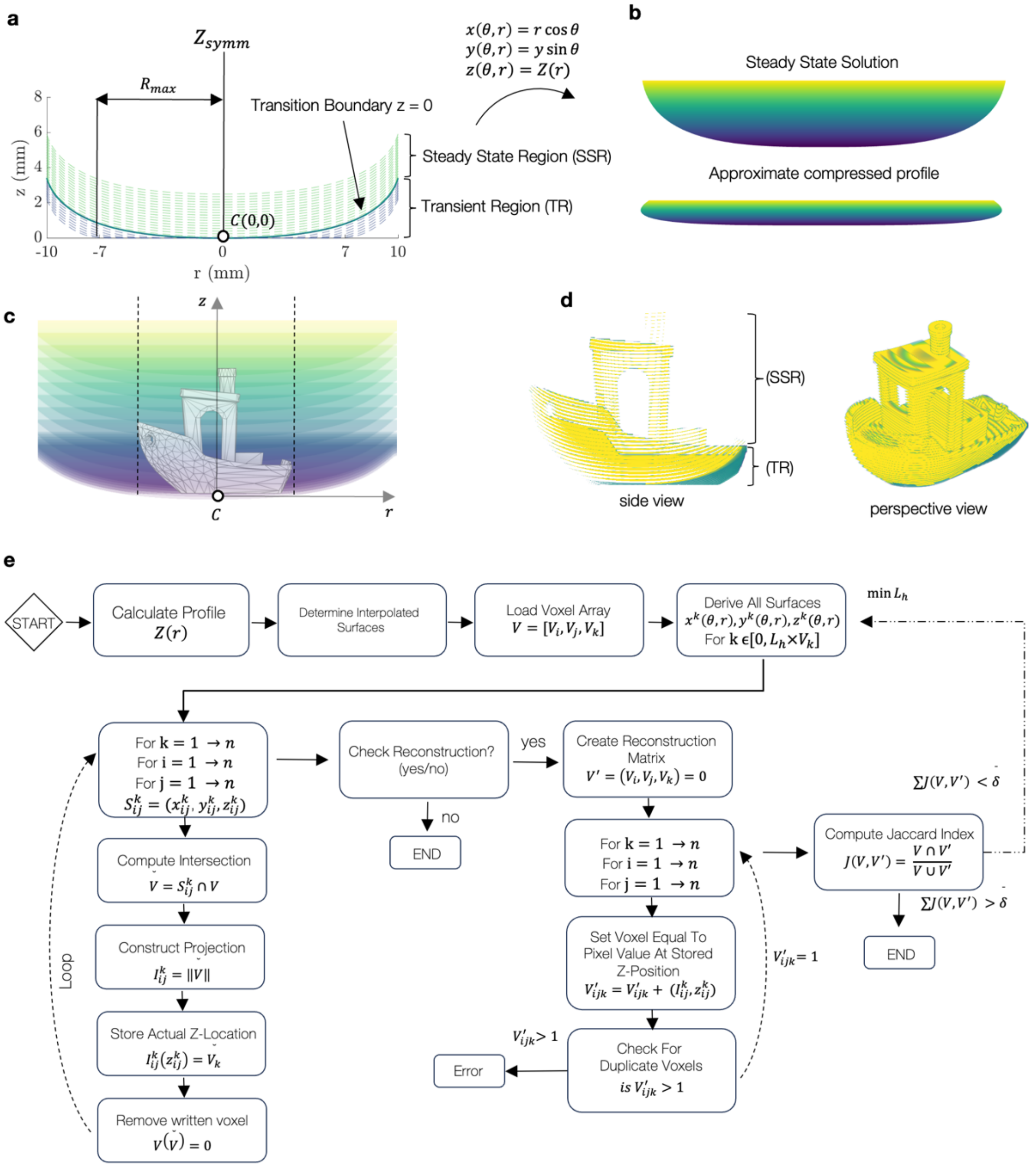

Supplementary Fig.5| Convex slicing algorithm process flow diagram. **a**, examples of interface profiles produced by the Young-Laplace interface model demonstrating the steady-state solution and transient region of the interface shape corresponding to compression about the contact point C. **b**, three-dimensional surface constructed by revolving the steady-state region and transient regions about the symmetry line Z_{symm}. **c**, overlay of the 'Benchy' model, which is a standard test geometry, with an array of meniscus profiles corresponding to the steady-state and transient solutions over the object's height. Note the number of surfaces shown is not representative of the total number normally used when printing. **d**, reconstruction of the Benchy model based on the projections from the convex slicing algorithm, low reconstruction quality is indicative of the limited number of slice planes. **e**, process-flow diagram of the slicing algorithm illustrating key steps in both the determination of convex projections I_{ij}^k and reconstruction validation via Jaccard Index $J(V, V')$.

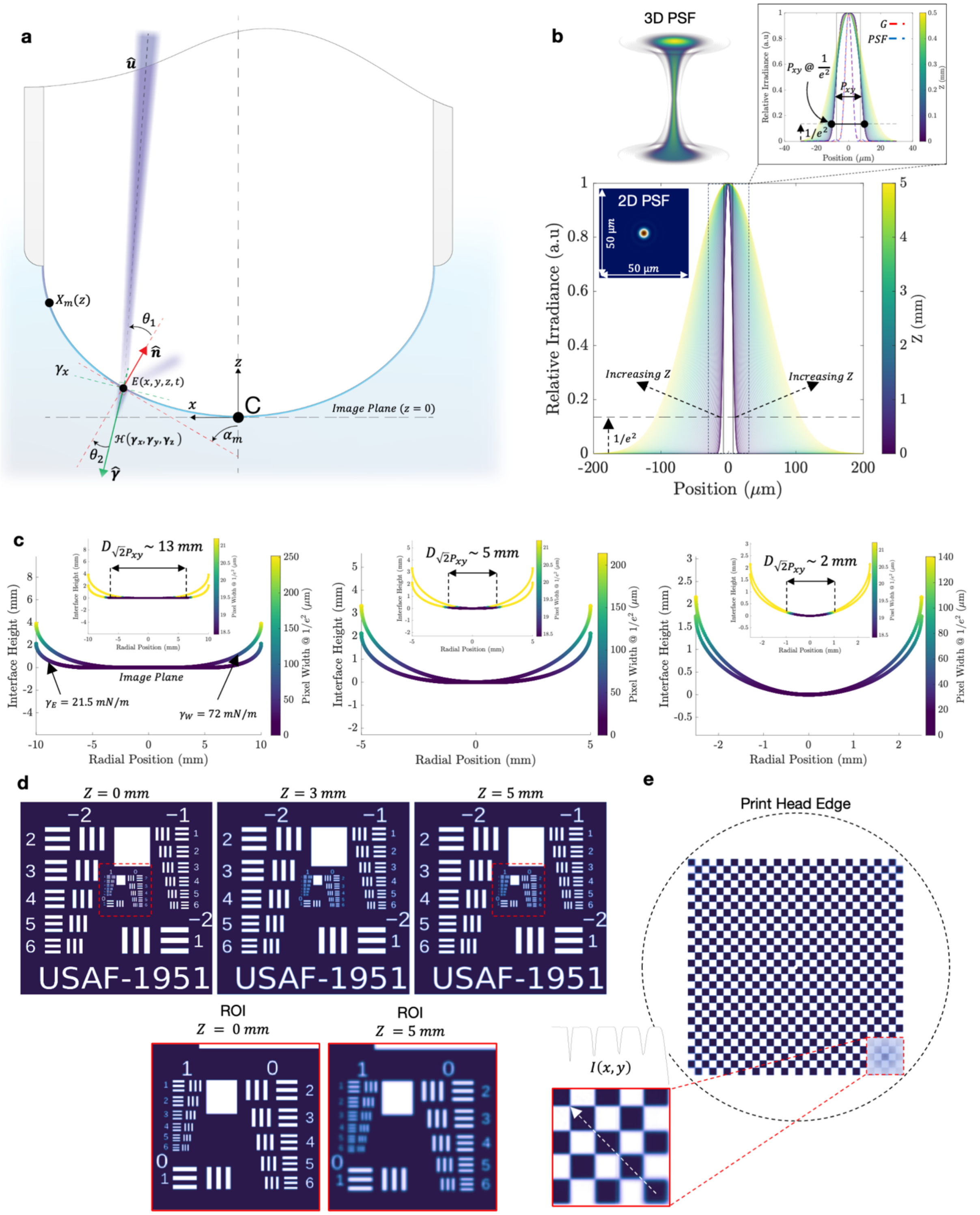

Supplementary Fig.6| Effect of interface curvature on in-plane resolution. **a**, optical coordinate system description denoting the incoming ray $\hat{u}$ and transmissive ray $\hat{\gamma}$ into the material. **b**, diverging effective pixel size P_{xy} across a z-depth of 0 – 5 mm. Insets show the effective pixel spread close to the focal plane, the corresponding 2D PSF at $z = 0$ and the approximate thresholded PSF in the range of $z = \pm 200\ \mu m$. **c**, effective pixel resolution across the meniscus boundary corresponding to D = 20 mm, D = 10 mm and D = 5 mm respectively, for a 90-degree contact angle ($\theta_Y = 90°$). Insets show the available printing area under the assumption of an allowable pixel divergence of $\sqrt{2}P_{xy}$. **d,** resultant USAF test pattern imaged at increasing planes above $z = 0$. Inset in red shows ROI at the centre of the test pattern at $z = 0$ and $z = 5$ respectively. **e**, total image distortion across the meniscus surface corresponding to the meniscus intersection with the 3D PSF.

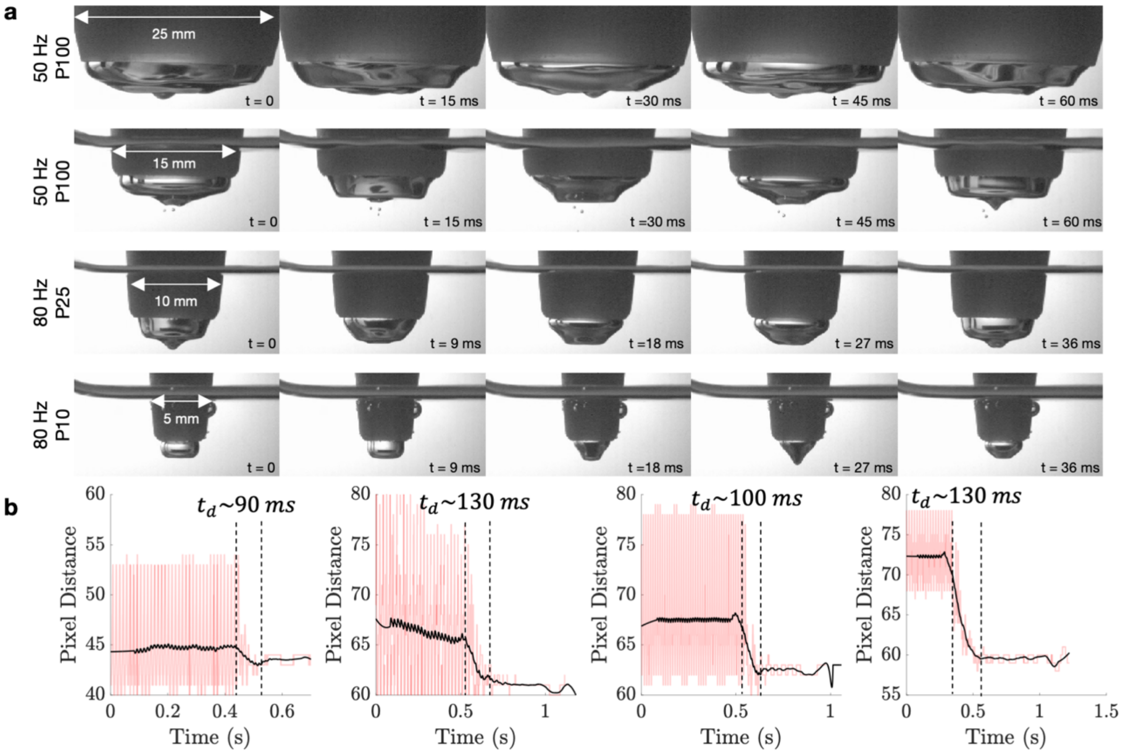

Supplementary Fig.7| Interface re-stabilization time as a function of print head diameter for PEGDA 20%. a, high contrast time-series images of the interface shape under high amplitude acoustic excitation. Each time series corresponds to approximately a single period of excitation. **b**, interface stabilization tracking for each of the print head configurations with decreasing print head size from left to right.

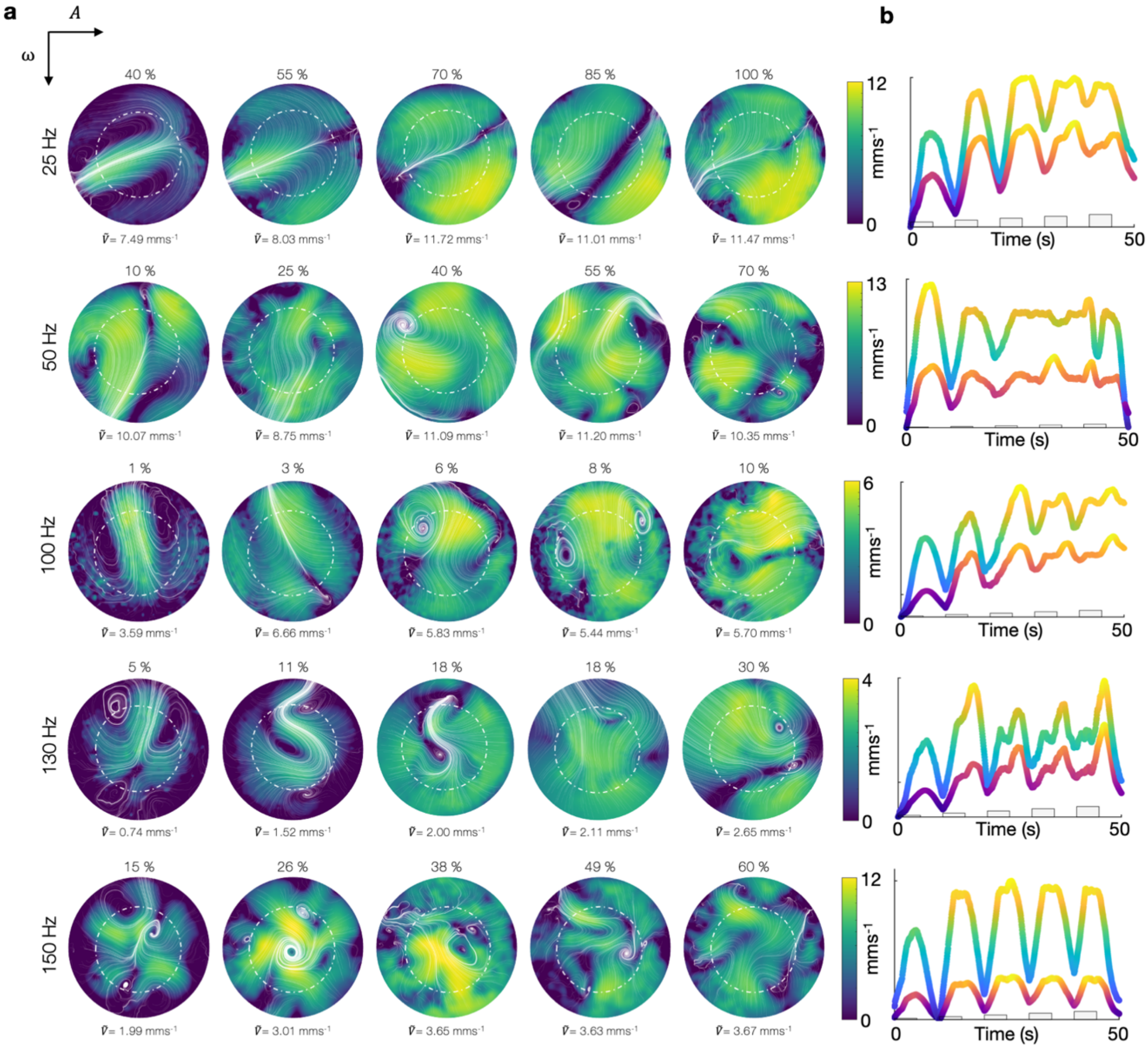

Supplementary Fig.8| Particle image velocimetry of the printing interface as imaged from above. **a**, time averaged velocity for 25 mm diameter print head with increasing driving amplitude A and frequency ω. Each image corresponds the average velocity across 20 frames, directly after acoustic actuation was turned off. $\tilde{V}$ denotes the average velocity within the centre 15 mm diameter region, highlighted by the white circular ring. **b**, average velocity and maximum velocity across the entire print field for each frequency and amplitude state. Grey bars indicate the time points and unit amplitude $(0 \rightarrow 1)$ of the acoustic stimulation, where each test corresponds to 5s of stimulation followed by 5s of no stimulation as shown.

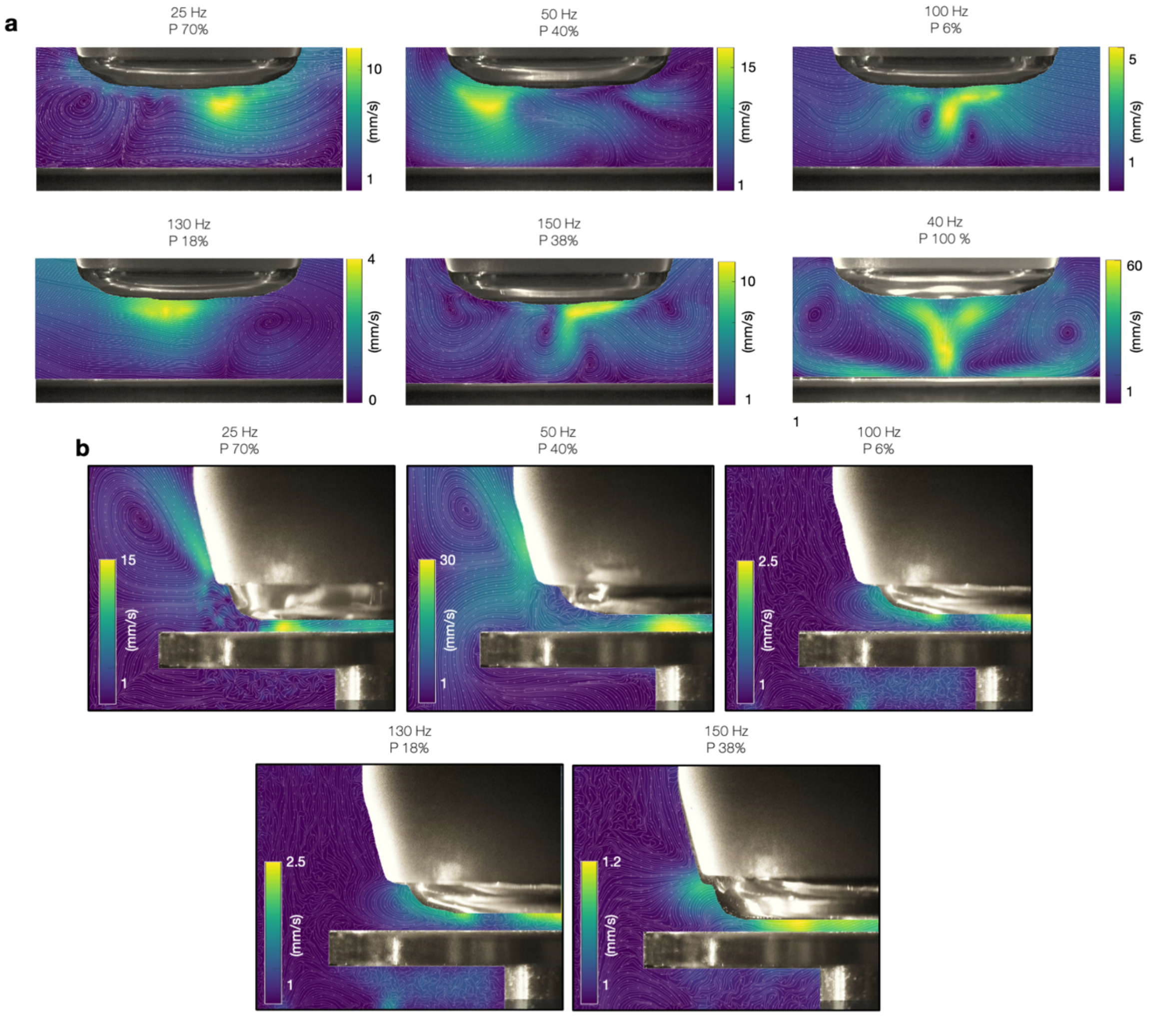

Supplementary Fig.9| Particle image velocimetry of the printing interface as imaged from the side. **a**, time-averaged velocity for 25 mm diameter print head for key driving frequency and amplitude pairs. Each image corresponds to the average velocity across 100 frames, with acoustic driving on for the entire test duration. The 40Hz P100 configuration highlights the ‘jetting’ ability of the interface under high amplitude, whereby a single high velocity jet can be formed at the centre of the print container. **b**, time averaged velocity near a solid boundary demonstrating that increased fluid velocity beyond bulk flow, can be seen under specific frequency conditions.

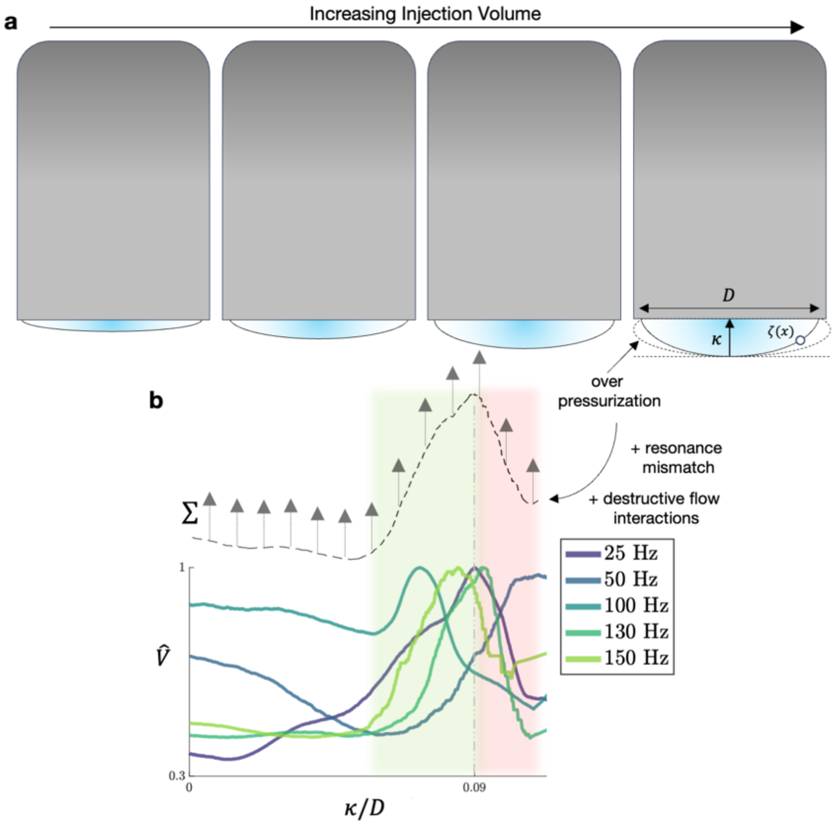

Supplementary Fig.10| Normalized fluid velocity for increasing meniscus curvature and extension κ. **a**, illustration of the parameter definitions for $\zeta(x)$, D and κ. **b**, normalized maximum velocity for κ/D over a range of driving frequencies for a fixed amplitude. Here $D = 25\ \mathrm{mm}$. Dotted line indicates the summation of all frequency response curves, emphasising a cumulative onset and peak velocity pairing, followed by a sharp decline in velocity due to over-pressurization, resonance mismatch and destructive flow interactions.

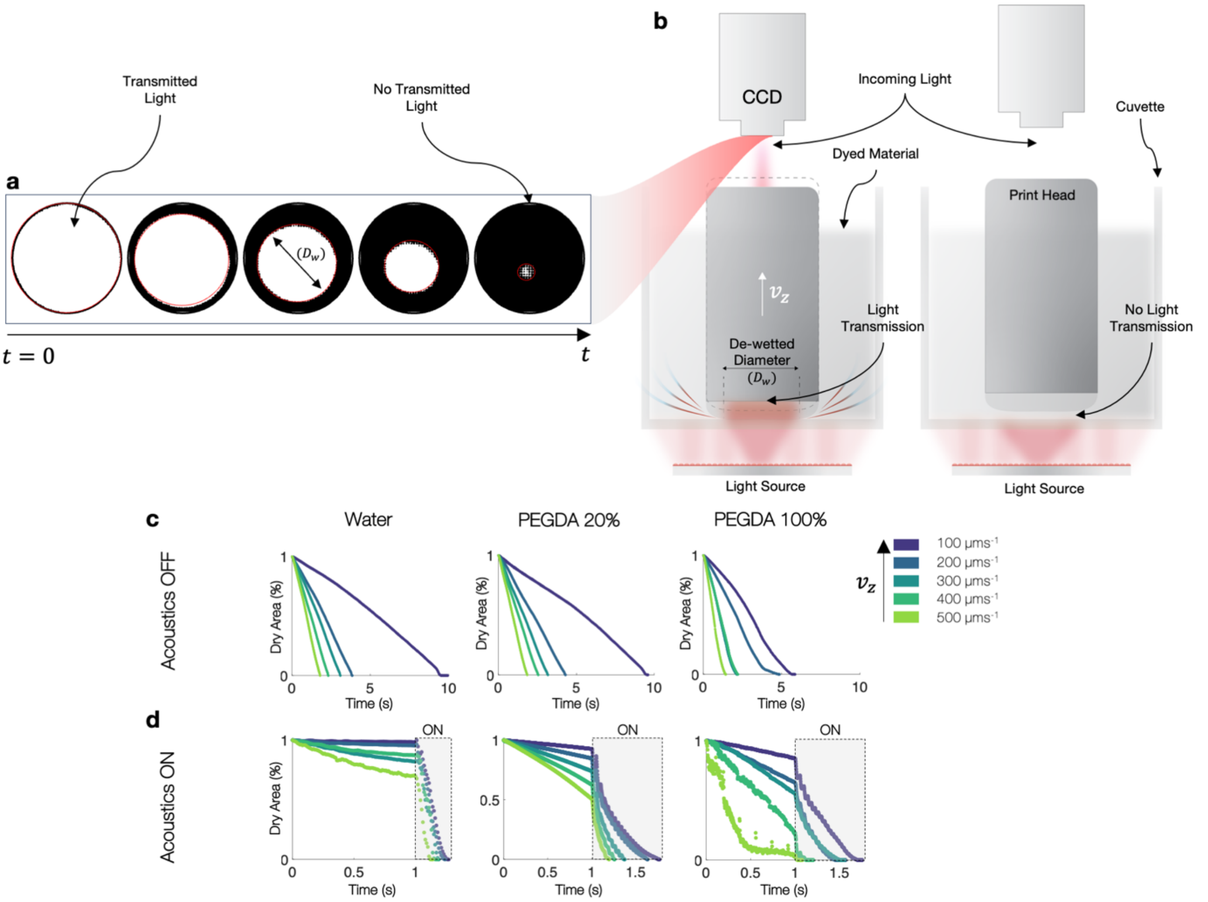

Supplementary Fig.11| Image based analysis of the material influx rate for the 25 mm print head with varying viscosity and surface tension values. a, time point images of the de-wetting of the meniscus as imaged from above. Dark regions of the image indicate interface release from the base of the cuvette, whereas light regions indicate interface contact resulting in light transmission. **b**, Schematic illustration of the optical setup used to capture the interface release dynamics. Each material was doped with a high concentration of black dye to attenuate the incoming light from the backlight. **c,** interface release dynamics without acoustic stimulation plotted for increasing rates of print head velocity v_z and PEGDA wt.% concentration. Dry area percentage corresponds to the area of the ellipsoid that encloses the transmitted light as a function of time, normalized against the initial area of the transmitted ellipsoid. **d**, interface release dynamics with acoustic stimulation, where $f = 50\ Hz$ and $A = 0.40$. In each case the print container was translated initially at the same rate as in **c** for 1 second, followed by enabling acoustic stimulation.

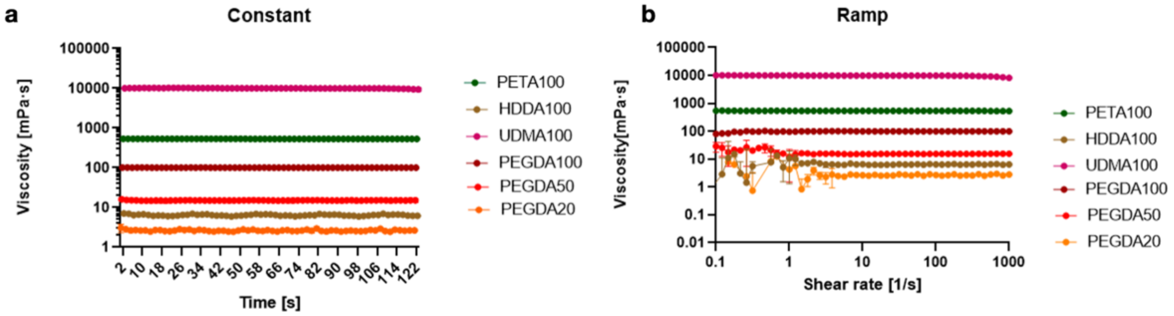

Supplementary Fig.12| Viscosity measurements for key materials investigated within this study. a, viscosity response under constant shear rate 10 (1/s). **b**, viscosity response under ramping shear rate from 0.01 to 1000 (1/s).

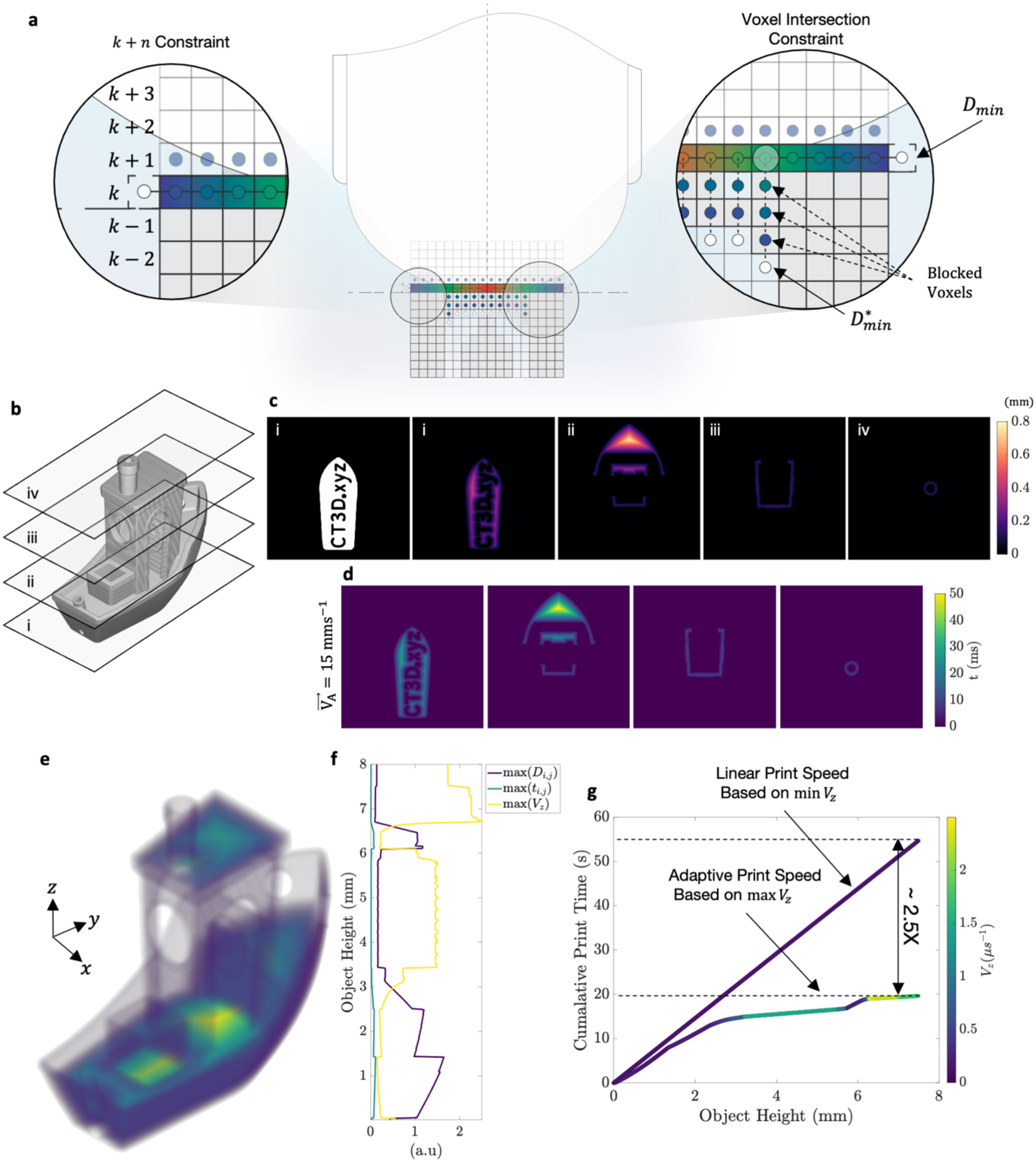

Supplementary Fig.13| Computational prediction of interface wetting time. **a**, illustration of algorithmic constraints applied to the 3D Euclidean distance calculation, where out of plane voxels above the calculation plane are not considered. Additionally, voxels whose distance minimizes the Euclidean distance function, but whose vector intersects with the voxel grid are also invalid solutions. **b**, voxelized Benchy model and corresponding computational target planes (i, ii, iii, iv). **c**, Euclidean distance transform applied to the corresponding target planes and normalized against the pixel size ($p_{x,y} = 15\ \mu\mathrm{m}$). **d**, interface wetting time in milliseconds for an acoustic flow velocity of $\overrightarrow{V_A} = 15\ \mathrm{mms}^{-1}$. **e**, 3D distance transform applied to the entire voxelised Benchy model, colormap represents the log magnitude of the minimum source distance in 3D with imposed constraints. **f**, maximum source distance $D_{i,j}$, infill time $t_{i,j}$ and achievable print velocity V_z, as a function of object height. **g**, comparison between linear and adaptive print speeds on the cumulative print time. Linear print speed was taken as the minimum calculated print speed over the entire object, whereas the adaptive print speed was determined instantaneously across the object height.

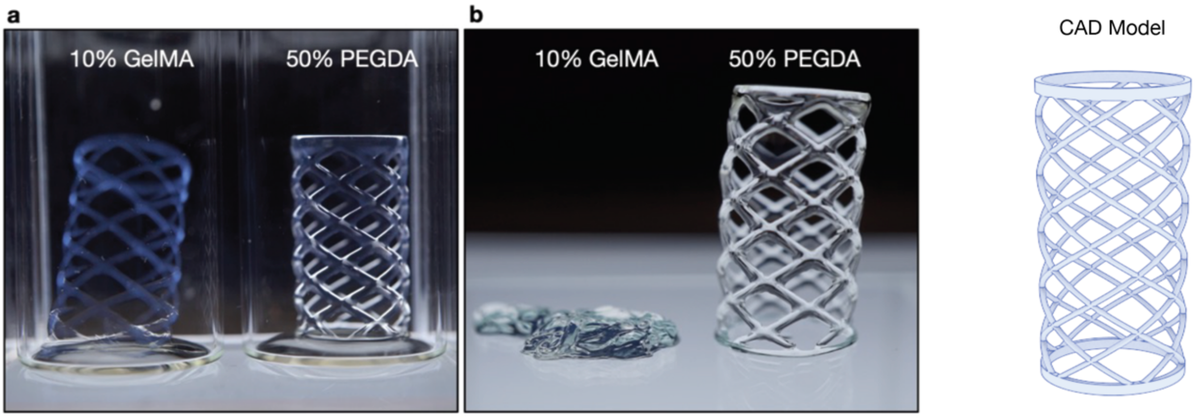

Supplementary Fig.14| Demonstration of in-situ liquid printing and its advantage for fabricating structures with low stiffness via dynamic interface printing. **a,** model of a helical stent geometry, constructed using a 10% GelMA hydrogel composition (left), juxtaposed with a counterpart fabricated from a 50% PEGDA composition (right). These structures, post-wash, are depicted in a liquid suspension. **b,** the GelMA and PEGDA structures after extraction from their supportive fluid, underscoring the remarkable range of stiffness that can be accomplished through the employment of DIP.

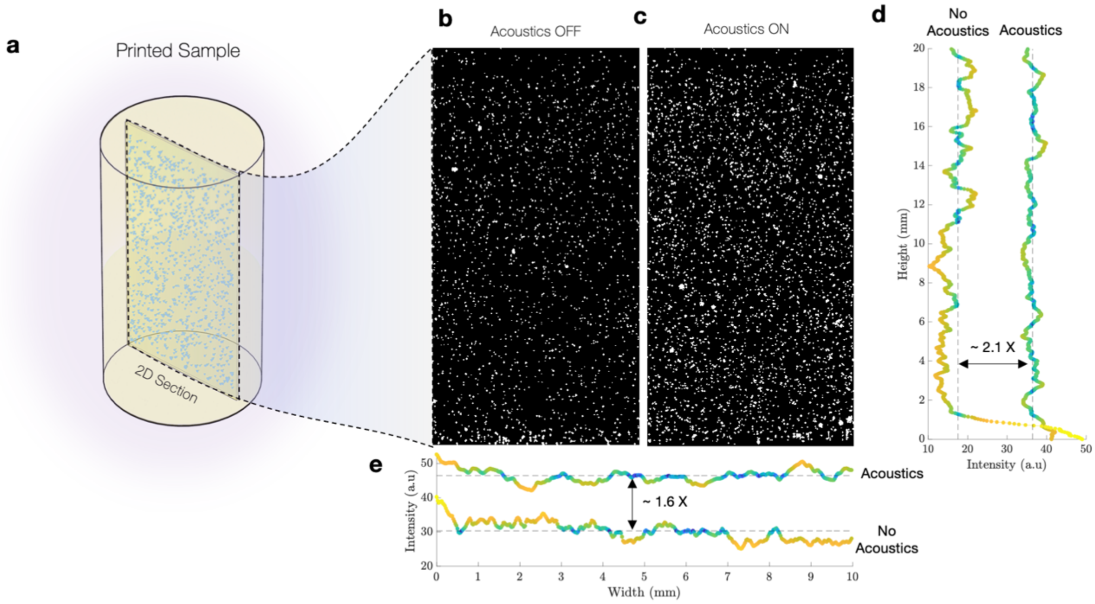

Supplementary Fig.15| Effect of acoustic stimulation on the settling of granular suspensions during printing. **a**, illustration of the sample geometry used for this investigation, whereby a circular geometry with a diameter of 10 mm was printed. **b**, 2D cross-section of the printed sample without acoustic stimulation. **c**, 2D cross-section of the printed sample with acoustic stimulation on with a frequency of 50Hz. **d**, summed thresholded intensity of the 2D cross-sectional image in the x-direction, highlighting that approximately 2.1X the number of particles were captured with acoustic actuation on, with a more consistent distribution of particles in the y-direction. **e**, summed thresholded intensity of the 2D cross-sectional image in the y-direction.

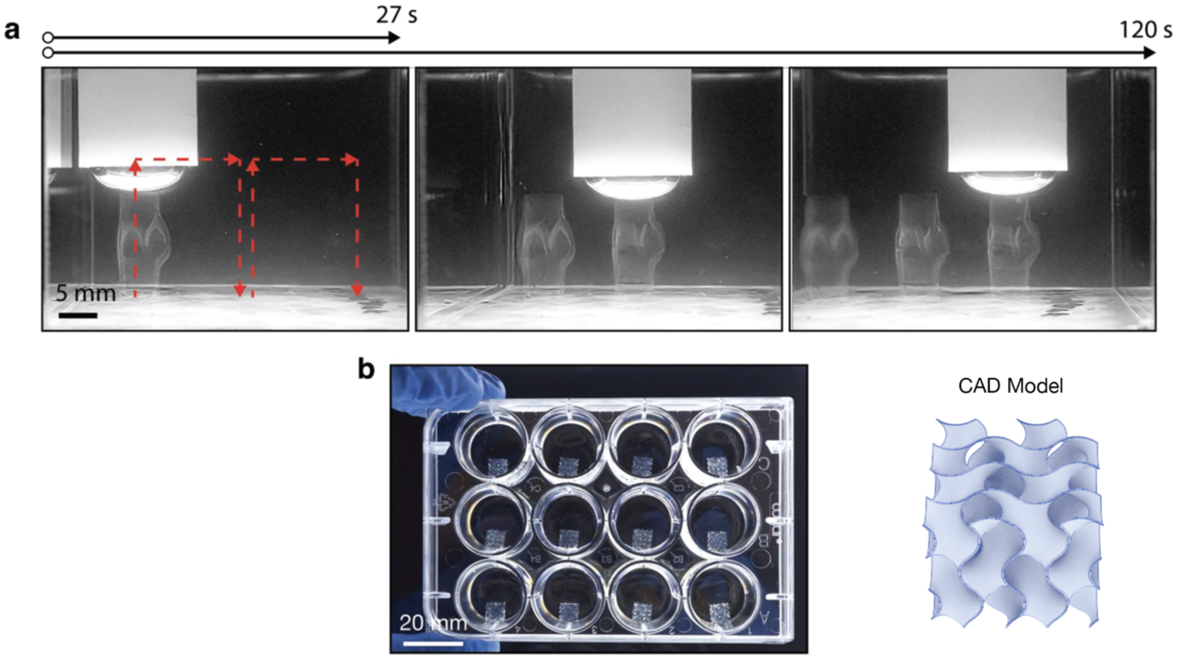

Supplementary Fig.16| Multi-step printing and direct in well printing. **a**, Time lapse images of three tricuspid valves printed in just under 120 seconds via three-dimensional placement of the print head. **b**, Direct in well printing of 12 gyroid lattices, created in just under 8 minutes.

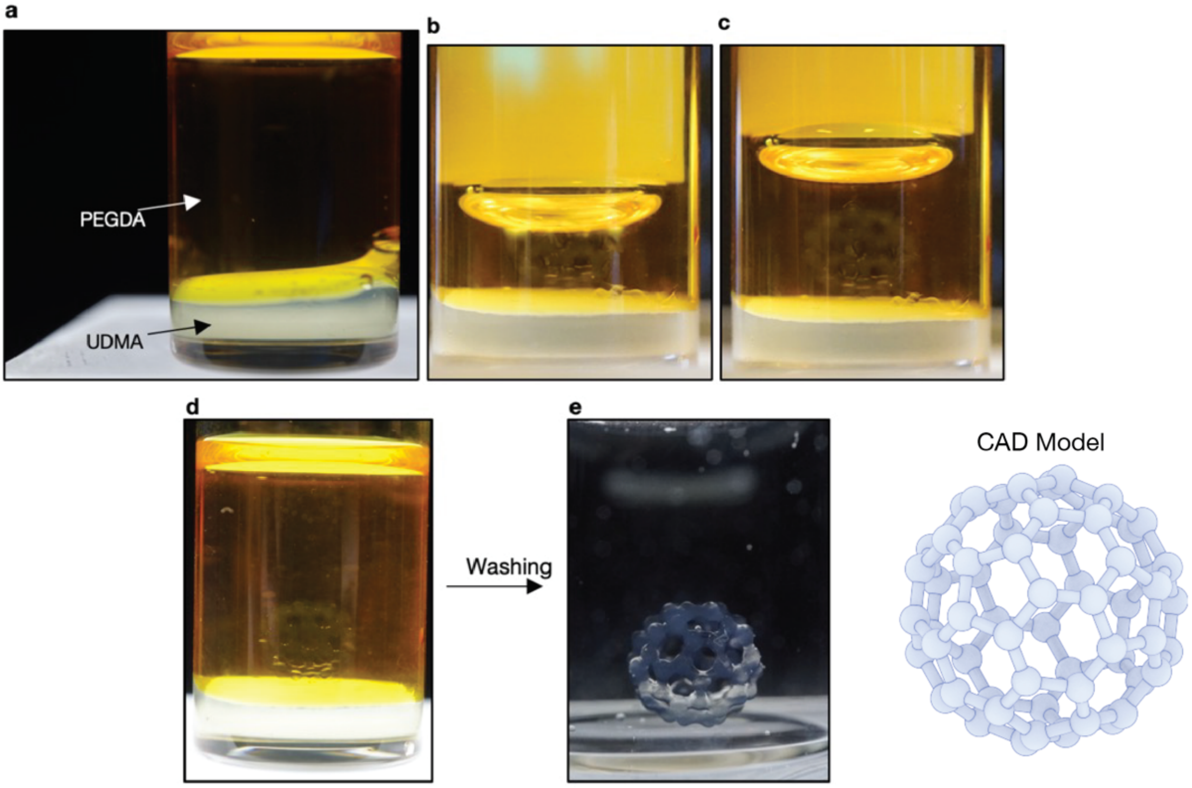

Supplementary Fig.17| Printing of free-floating structures by utilizing high viscosity dense materials. a, UDMA and PEGDA loaded into a 15 mm diameter vial. **b,** Bucky-ball structure during printing whereby the high viscosity UDMA acts as a fluidic supporting medium. **c-d**, Bucky-ball directly after printing. **e**, Bucky-ball (C60) after removal of UDMA and PEGDA.

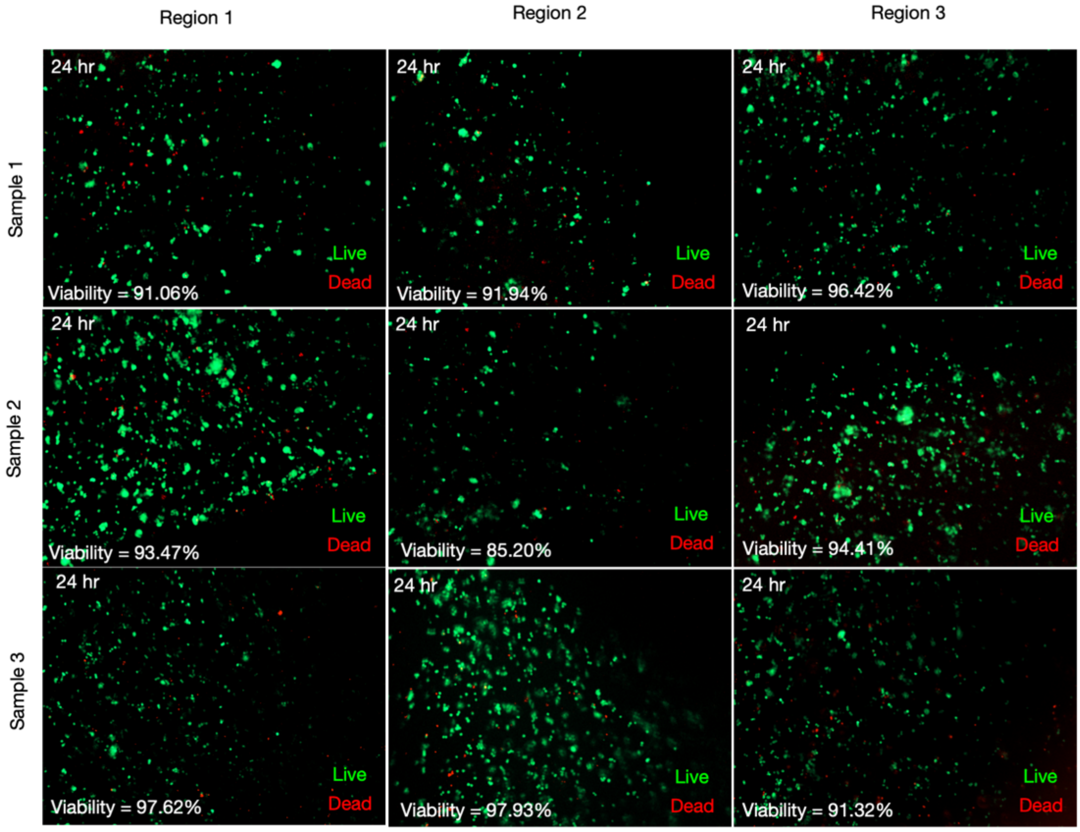

Supplementary Fig.18| Triplicate florescence images of the wall test structure for three representative regions at 24h after printing. High cell viability demonstrates no immediate cytotoxicity due to DIP printing. Average cell viability across the samples is 93.26% after 24h.

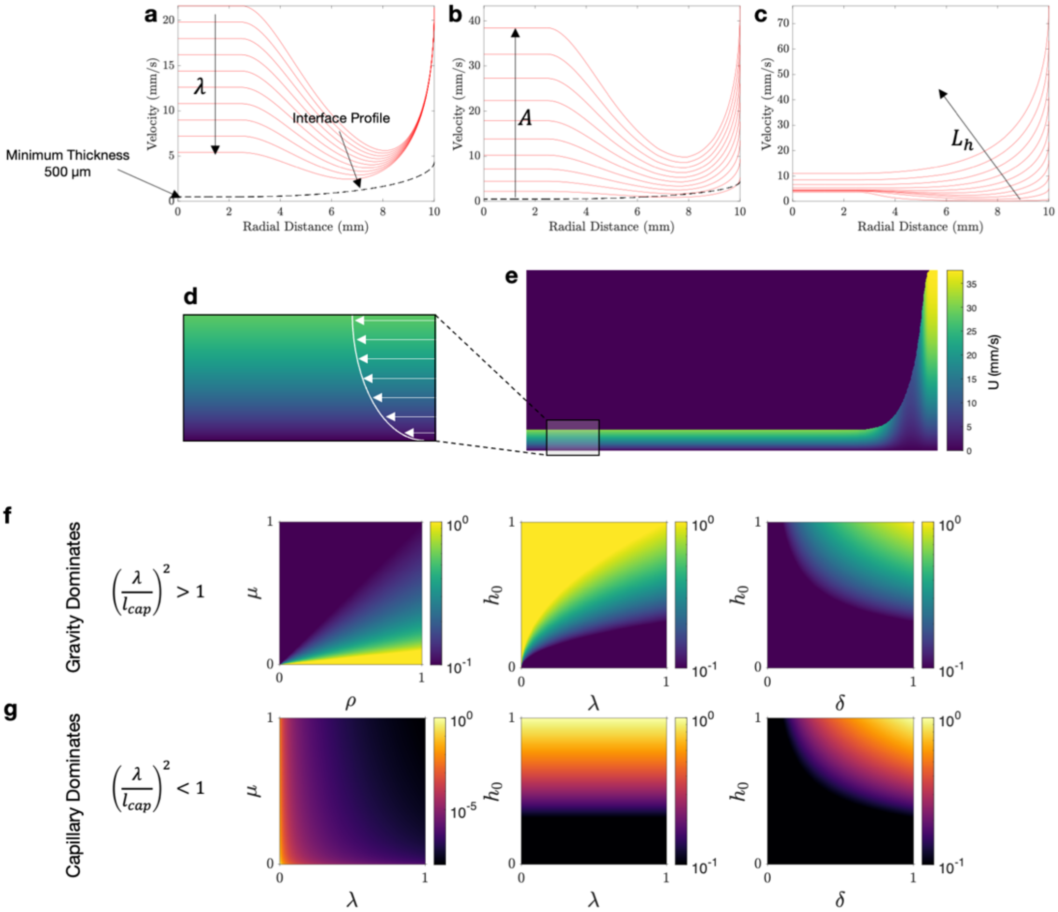

Supplementary Fig.19| Analytical analysis of the effect of material and interface properties on acoustically driven flow profiles. **a**, Effect of decreasing acoustic wavelength on maximum flow velocity in the x-direction as a function of the profile height. The chosen interface profile was derived from the Young-Laplace solution for PEGDA 20%. **b**, Effect of increasing the driving amplitude on the maximum flow velocity in the x-direction as a function of the interface height. **c**, Effect of increasing the layer height (gap between the interface and the lower surface) on the maximum flow velocity in the x-direction. **d**, 2D flow profile below the interface with a layer height thickness of 500 µm. **d**, 2D flow profile of the interface entire interface. **f**, dimensionless exploration of how material properties affect the velocity in the x-direction for a gravity dominated system $(\lambda/l_{cap})^2 > 1$. Velocity scaling is shown on a log scale. **g**, dimensionless exploration of how material properties affect the velocity in the x-direction for a capillary dominated system $(\lambda/l_{cap})^2 < 1$. Velocity scaling is shown on a log scale.

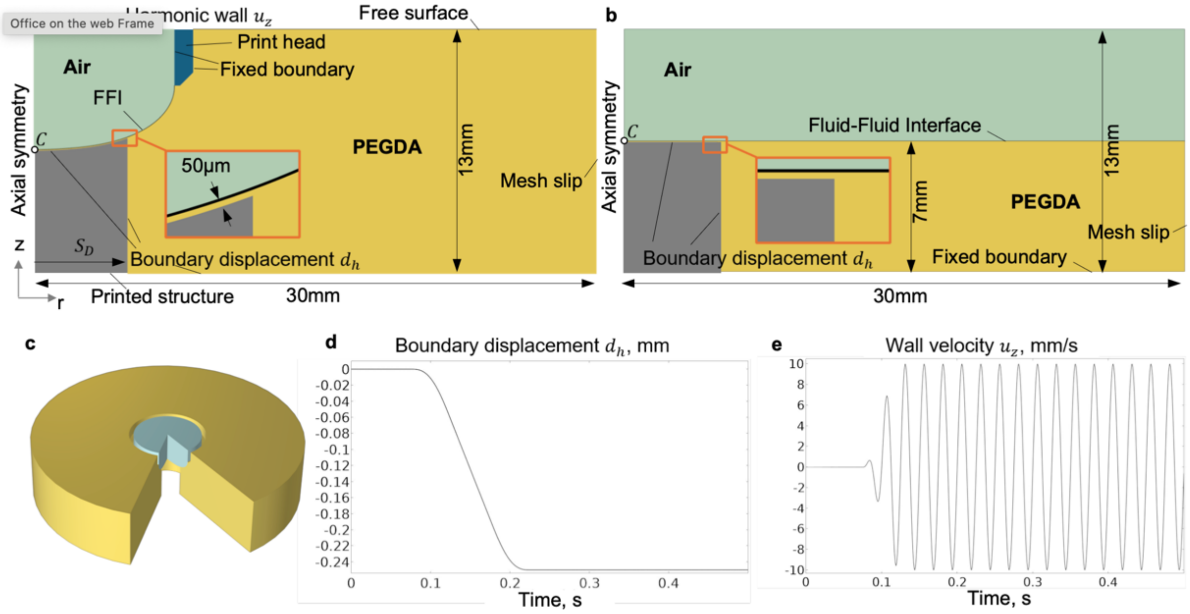

Supplementary Fig.20| Finite element analysis (FEA) and numerical setup of resin influx across printed structure. **a**, Graphical view of the axisymmetric computational domain for DIP. **b**, 3D representation of the DIP simulation domain revolved around the z-axis. **c**, The view of the DIP computational domain. **d**, Modelling domain boundary displacement. **e**, Temporal evolution of the wall velocity for the acoustically actuated DIP.

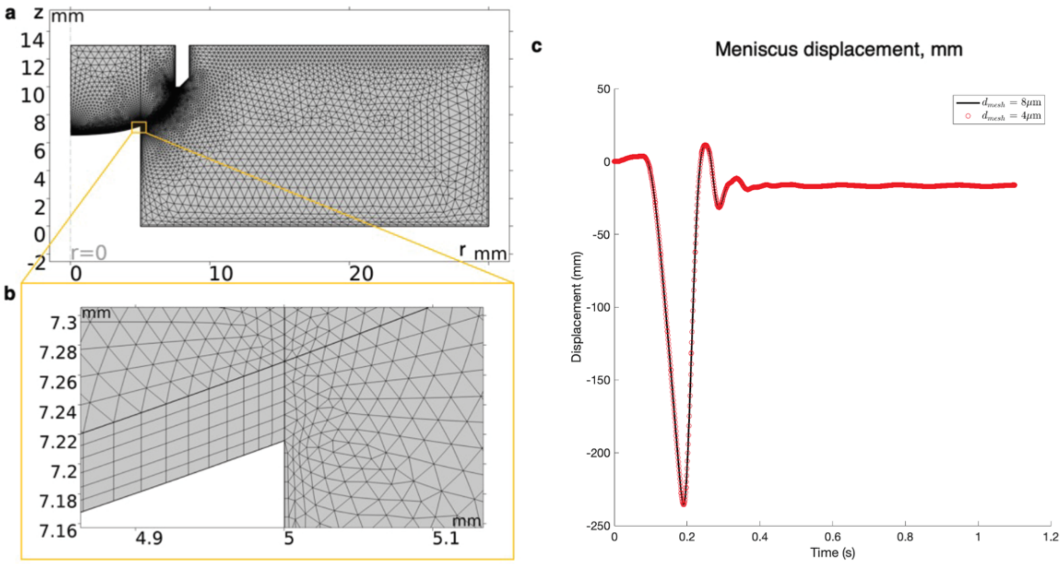

Supplementary Fig.21| Computational mesh and mesh refinement study used for the numerical modelling. a, Computational mesh with element size $\mathrm{d_{mesh}} = 8$ μm. **b**, A magnified view of the mesh. **c**, The displacement of the meniscus over time yields comparable results if a refined mesh is utilized.

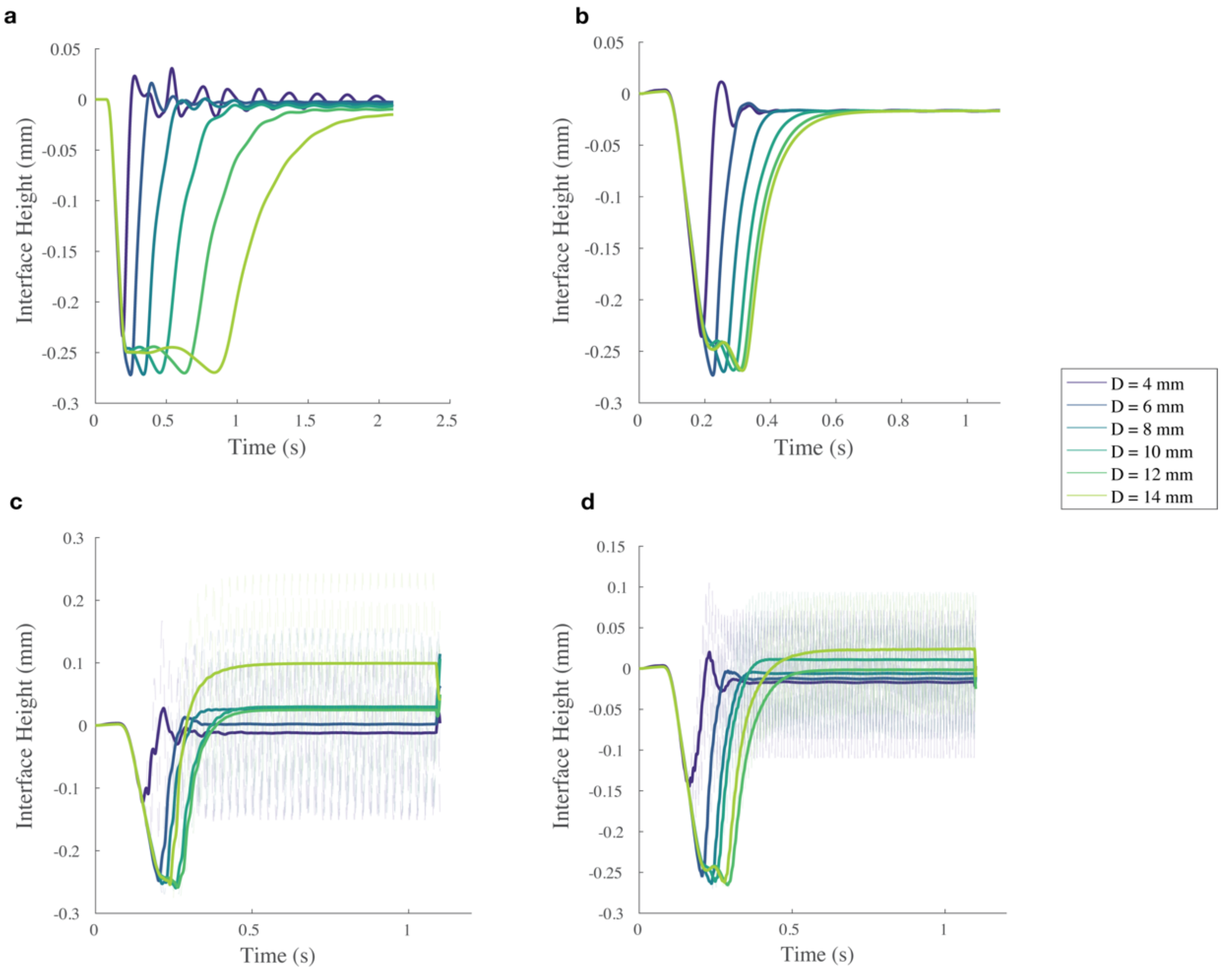

Supplementary Fig.22| Numerical prediction of the interface release dynamics for a 15 mm diameter print head with varying circular printed structures ranging from 4 to 14 mm in diameter. a, Location of the central node of the interface as a function of time for Top-Down SLA. **b,** Location of the central node of the interface as a function of time for Dynamic Interface Printing (DIP) without acoustic excitation. **c,** Location of the central node of the interface as a function of time for Dynamic Interface Printing (DIP) with acoustic excitation at a frequency of 40 Hz. **d,** Location of the central node of the interface as a function of time for Dynamic Interface Printing (DIP) with acoustic excitation at a frequency of 100 Hz. For (**c-d**) the transparent plots denote the oscillatory interface height, with the solid lines representing the moving average across a single excitation period.

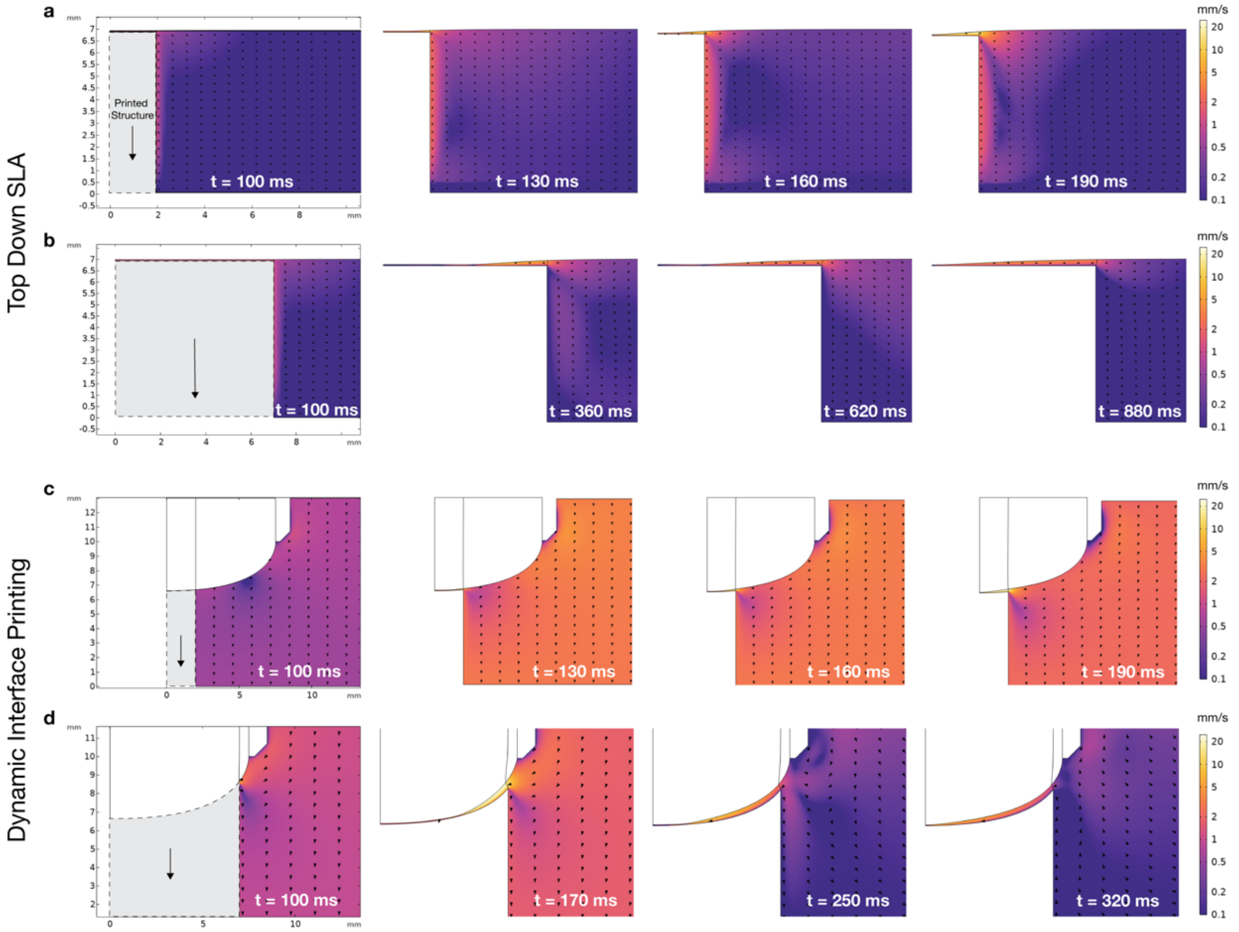

Supplementary Fig.23| Numerical prediction of the velocity magnitude for top-down SLA compared to dynamic interface printing with a 15 mm diameter print head. a, Time sequence velocity field for top-down SLA from the time of initial displacement (t = 100ms) to central interface release (t = 190 ms) for a 4 mm diameter printed structure. **b,** Time sequence velocity field for top-down SLA from the time of initial displacement (t = 100ms) to central interface release (t = 880 ms) for a 14 mm diameter printed structure. **c,** Time sequence velocity field for dynamic interface printing without acoustics from the time of displacement (t = 100ms) to central interface release (t = 190 ms) for a 4 mm diameter printed structure. **d,** Time sequence velocity field for dynamic interface printing without acoustics from the time of displacement (t = 100ms) to central interface release (t = 320 ms) for a 14 mm diameter printed structure. Velocity magnitude for each contour plot is indicated on the right-hand side of each row. Logarithmic colormap was chosen to indicate the global flow field more effectively.

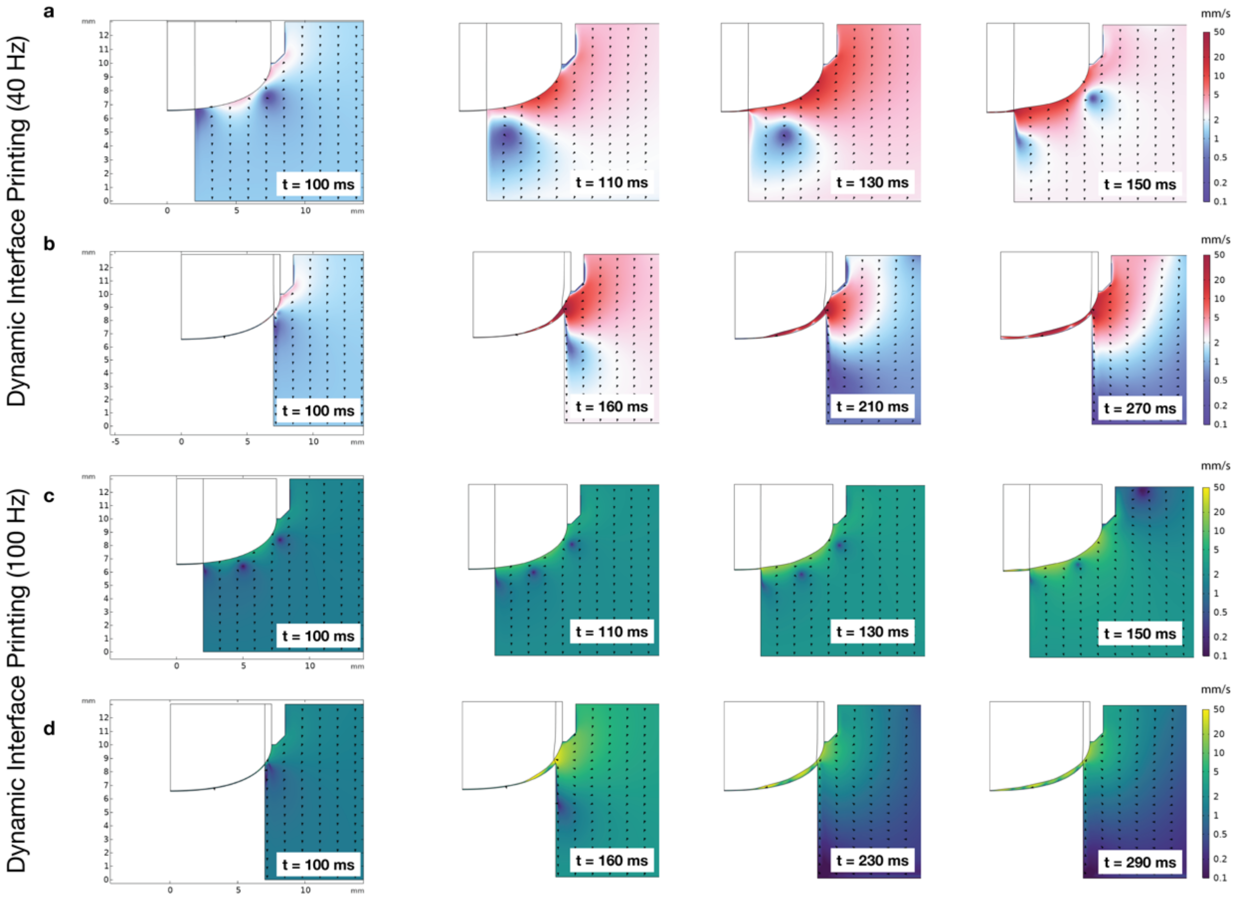

Supplementary Fig. 24 | Numerical prediction of the velocity magnitude for acoustically driven dynamic interface printing using a 15 mm diameter print head. a, Time-sequence velocity field for acoustically driven dynamic interface printing at a frequency of 40 Hz and a structural diameter of 4 mm. The time sequence spans from the initial displacement (t = 100 ms) to the central interface release (t = 150 ms). **b,** Time-sequence velocity field for acoustically driven dynamic interface printing at a frequency of 40 Hz and a structural diameter of 14 mm. The time sequence spans from the initial displacement (t = 100 ms) to the central interface release (t = 270 ms). **c,** Time-sequence velocity field for acoustically driven dynamic interface printing at a frequency of 100 Hz and a structural diameter of 4 mm. The time sequence spans from the initial displacement (t = 100 ms) to the central interface release (t = 150 ms). **d,** Time-sequence velocity field for acoustically driven dynamic interface printing at a frequency of 100 Hz and a structural diameter of 14 mm. The time sequence spans from the initial displacement (t = 100 ms) to the central interface release (t = 290 ms). Velocity magnitude for each contour plot is indicated on the right-hand side of each row. Logarithmic colormap was chosen to indicate the global flow field more effectively.

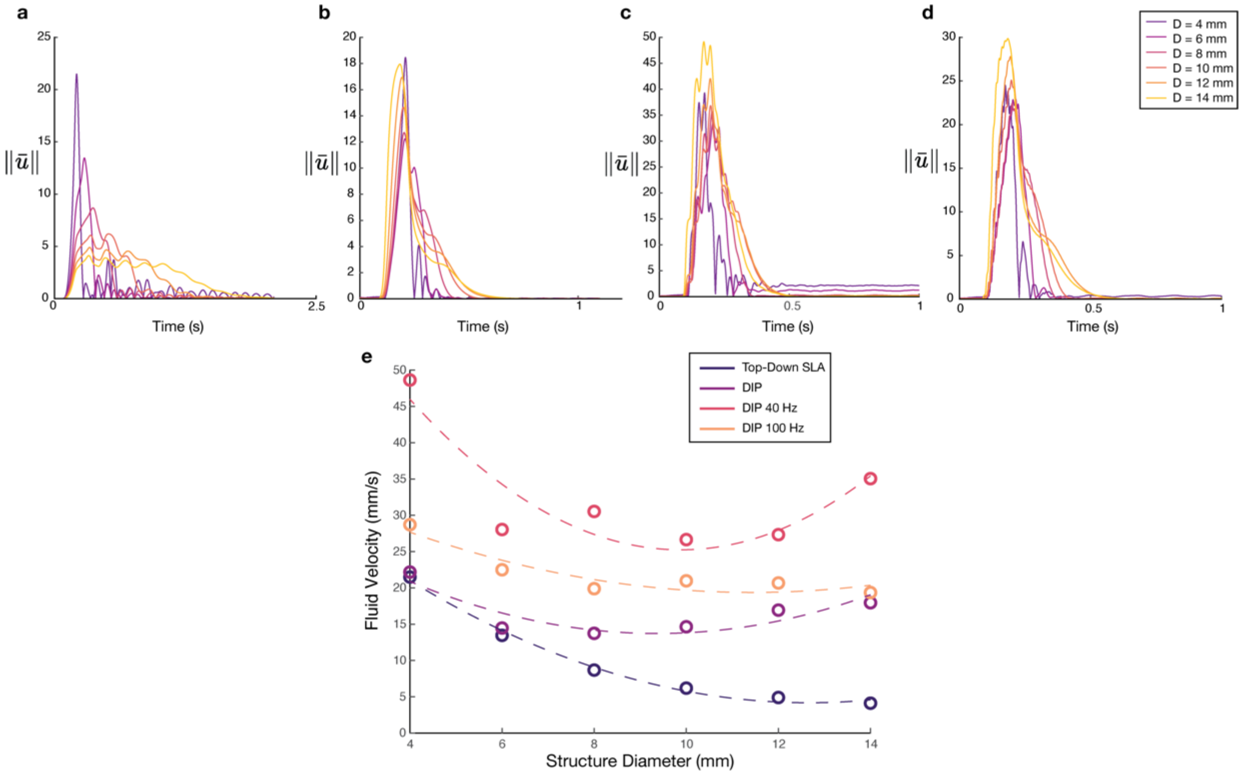

Supplementary Fig.25| Numerical prediction of the average inflow fluid velocity for a 15 mm diameter print head with varying circular printed structures ranging from 4 to 14 mm in diameter. a, Radial magnitude of the average fluid velocity ($\|\bar{u}\|$) for increasing structural diameter in top-down SLA. **b,** Radial magnitude of the average fluid velocity ($\|\bar{u}\|$) for increasing structural diameter in DIP without acoustics. **c,** Radial magnitude of the average fluid velocity ($\|\bar{u}\|$) for increasing structural diameter in DIP with 40 Hz acoustic driving. **d,** Radial magnitude of the average fluid velocity ($\|\bar{u}\|$) for increasing structural diameter in DIP with 100 Hz acoustic driving. **e**, Peak average fluid velocity for each printing technique as a function of structural diameter.

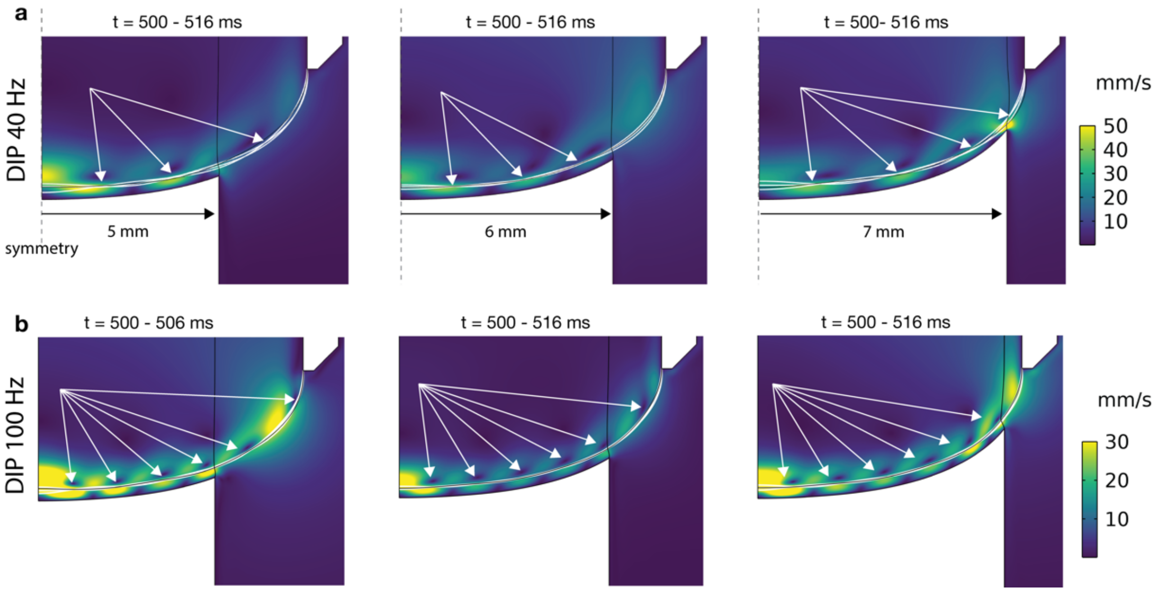

Supplementary Fig. 26| Numerical prediction of structural-modal interaction for acoustically driven dynamic interface at 40Hz and 100 Hz. a, Meniscus resonance mode shapes (indicated in white solid lines) over a single period at 40 Hz acoustic driving for structures with diameters of 10, 12, and 14 mm. **b,** Meniscus resonance mode shapes (indicated in white solid lines) over a single period at 100 Hz acoustic driving for structures with diameters of 10, 12, and 14 mm. White arrows indicate the locations of the nodal locations of the induced capillary wave. Linear colormap indicates the magnitude of the velocity field both within the fluid and within the enclosed air volume above the meniscus.

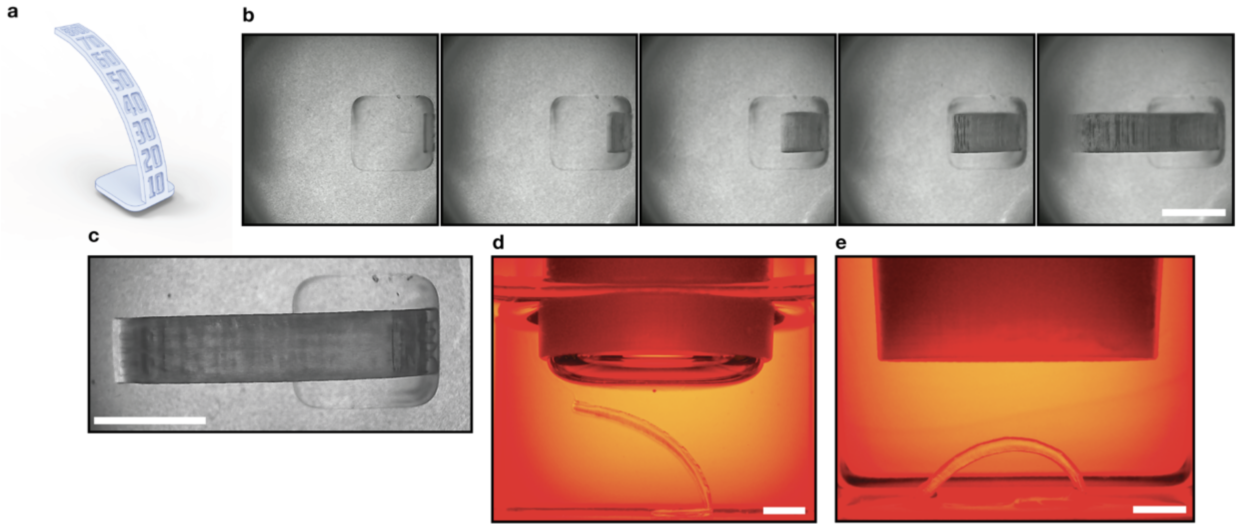

Supplementary Fig.27| DIP printing of an overhang test structure with angles ranging from 10°- 80° in PEGDA 20%. a, CAD model of the overhang test structure. **b**, Timelapse imaging of the test structure fabrication. **c**, Closeup image from above after fabrication. **d**, Side view after fabrication. **e**, Collapse of the test structure after the removal of the surrounding material. All scale bars are 5 mm.

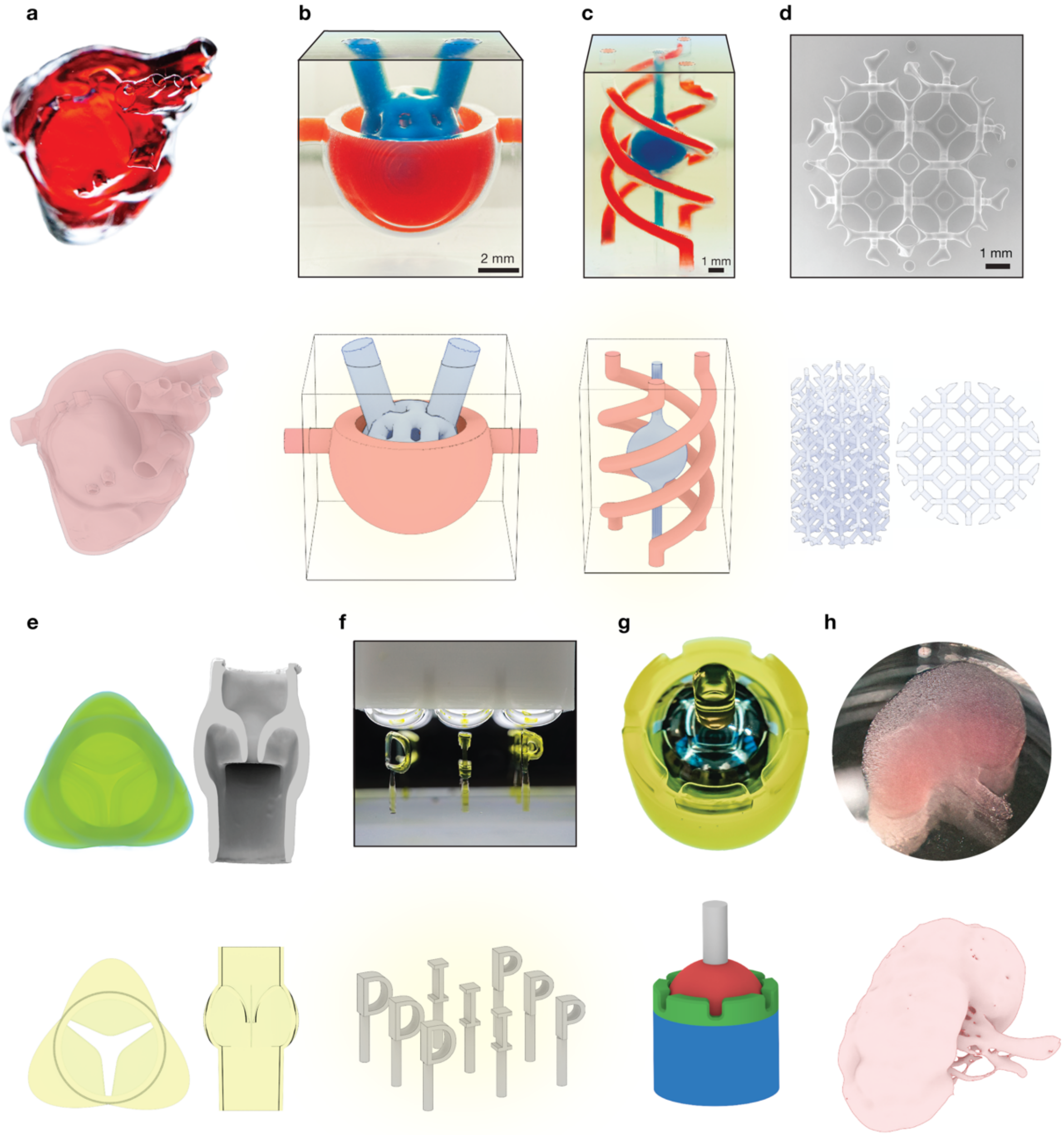

Supplementary Fig.28| Comparison of the printed structures with their corresponding CAD models, as presented in the main text. a, Printed heart model. **b**, Bowmans Capsule. **c**, Tri-helix. **d**, Kelvin cell lattice. **e**, Tricuspid valve. **f**, Letters ‘DIP’. **g**, Ball and socket joint. **h**, Anatomical kidney.

Material	Viscosity (mPas)	Surface Tension (mN/m)
PEGDA 20	2.75	64.82 (estimated)
PEGDA 50	15.23	52.85 (estimated)
PEGDA 100	100.50	32.90
HDDA	6.45	33.20
UDMA	9736	37.60

Supplementary Table 1| Viscosity and surface tension values for key materials explored in this work.

References:

1. Butt, H. J. et al. Characterization of super liquid-repellent surfaces. Current Opinion in Colloid and Interface Science vol. 19 Preprint at https://doi.org/10.1016/j.cocis.2014.04.009 (2014).
2. Statics: including Hydrostatics and the Elements of the Theory of Elasticity. Nature 116, (1925).
3. Zhang, Z. & Joshi, S. An improved slicing algorithm with efficient contour construction using STL files. International Journal of Advanced Manufacturing Technology 80, (2015).
4. Lewis, K. & Matsuura, T. Bézier Curve Method to Compute Various Meniscus Shapes. ACS Omega 8, 15371–15383 (2023).
5. Lewis, K. & Matsuura, T. Calculation of the Meniscus Shape Formed under Gravitational Force by Solving the Young–Laplace Differential Equation Using the Bézier Curve Method. ACS Omega 7, 36510–36518 (2022).
6. Andrzejewska, E. Photopolymerization kinetics of multifunctional monomers. Progress in Polymer Science (Oxford) vol. 26 Preprint at https://doi.org/10.1016/S0079-6700(01)00004-1 (2001).
7. Eelbode, T. et al. Optimization for Medical Image Segmentation: Theory and Practice When Evaluating With Dice Score or Jaccard Index. IEEE Trans Med Imaging 39, (2020).
8. Behroodi, E., Latifi, H. & Najafi, F. A compact LED-based projection microstereolithography for producing 3D microstructures. Sci Rep 9, 19692 (2019).
9. Jacobs, P. F. Fundamentals of stereolithography. in 1992 International Solid Freeform Fabrication Symposium (1992).
10. Hecht, E. Hecht optics. Addison Wesley vol. 997 Preprint at (1998).
11. Born, M., Wolf, E. & Hecht, E. Principles of Optics: Electromagnetic Theory of Propagation, Interference and Diffraction of Light . Phys Today 53, (2000).
12. Hsiao, K. et al. Single-digit-micrometer-resolution continuous liquid interface production. Sci Adv 8, (2022).
13. Tumbleston, J. R. et al. Continuous liquid interface production of 3D objects. Science (1979) 347, 1349–1352 (2015).
14. Basic lubrication theory. Wear 84, (1983).
15. Porte, E., Cann, P. & Masen, M. A lubrication replenishment theory for hydrogels. Soft Matter 16, (2020).
16. Oron, A., Davis, S. H. & Bankoff, S. G. Long-scale evolution of thin liquid films. Rev Mod Phys 69, (1997).
17. Zhang, X. Observations on waveforms of capillary and gravity-capillary waves. European Journal of Mechanics, B/Fluids 18, (1999).
18. Périnet, N., Gutiérrez, P., Urra, H., Mujica, N. & Gordillo, L. Streaming patterns in Faraday waves. J Fluid Mech 819, (2017).
19. Huang, Y., Wolfe, C. L. P., Zhang, J. & Zhong, J. Q. Streaming controlled by meniscus shape. J Fluid Mech 895, (2020).
20. Dendukuri, D. et al. Modeling of oxygen-inhibited free radical photopolymerization in a PDMS microfluidic device. Macromolecules 41, (2008).
21. Elizondo-Leal, J. C. et al. Parallel raster scan for euclidean distance transform. Symmetry (Basel) 12, (2020).
22. Sramek, M. & Kaufman, A. Fast ray-tracing of rectilinear volume data using distance transforms. IEEE Trans Vis Comput Graph 6, 236–252 (2000).
23. Amanatides, J. & Woo, A. A Fast Voxel Traversal Algorithm for Ray Tracing. Eurographics 87, (1987).